Bifurcation analysis and frequency prediction in shear-driven cavity flow

Y. Bengana[1], J.-Ch. Loiseau[2], J.-Ch. Robinet[2] and L. S. Tuckerman[1]†

[1]Laboratoire de Physique et Mécanique des Milieux Hétérogènes (PMMH), CNRS; ESPCI Paris, PSL Research University; Sorbonne Université; Univ. Paris Diderot, France

[2]Laboratoire DynFluid, Arts et Métiers ParisTech, 75013 Paris, France

A comprehensive study of the two-dimensional incompressible shear-driven flow in an open square cavity is carried out. Two successive bifurcations lead to two limit cycles with different frequencies and different numbers of vortices which propagate along the top of the cavity and circulate in its interior. A secondary bifurcation to a quasiperiodic state mediates the stability of these limit cycles. A full analysis of this scenario is obtained by means of nonlinear simulations, linear stability analysis, and Floquet analysis. We characterize the temporal behavior of the limit cycles and quasiperiodic state via Fourier transforms and their spatial behavior via the Hilbert transform. We address the relevance of linearization about the mean flow. Although here the nonlinear frequencies are not very far from those obtained by linearization about the base flow, the difference is substantially reduced when eigenvalues are obtained instead from linearization about the mean and in addition, the corresponding growth rate is small, a combination of properties called RZIF. Moreover growth rates obtained by linearization about the mean of one limit cycle are correlated with relative stability to the other limit cycle. Finally, we show that the frequencies of the successive modes are separated by a constant increment.

1. Introduction

We consider the incompressible shear-driven flow in a cavity, also known as open cavity flow. This is a geometrically induced separated boundary layer flow which has a number of applications in aeronautics (Yu 1977) and in industry, where it can serve as a mixing device (Chien *et al.* 1986). The first two-dimensional instability of the flow is primarily localized along the shear layer delimiting the outer boundary layer and the inner cavity (Sipp & Lebedev 2007; Sipp *et al.* 2010). This instability relies essentially on two mechanisms. First, the convectively unstable nature of the shear layer causes perturbations to grow as they travel downstream. Once they impinge on the downstream corner of the cavity, the inner-cavity recirculating flow and the instantaneous pressure feedback provide the mechanisms by which these perturbations re-excite the upstream portion of the shear layer. At sufficiently high Reynolds numbers, the coupling of these mechanisms gives rise to a linearly unstable feedback loop. A similar unstable loop exists for compressible shear-driven cavity flows in which the instantaneous pressure feedback is replaced by upstream-propagating acoustic waves (Rossiter 1964; Rockwell & Naudascher 1978; Rowley *et al.* 2002; Gloerfelt 2009; Yamouni *et al.* 2013).

This two-dimensional linearly unstable flow configuration has also served multiple theoretical modeling purposes over the past decade: the illustration of optimal control and reduced-order modeling (Barbagallo *et al.* 2009; Loiseau & Brunton 2018), and as

† Email address for correspondence: laurette@pmmh.espci.fr

an introduction to dynamic mode decomposition (Schmid 2010). Most relevant to the present work is the use of this configuration to investigate the prediction of frequencies from the mean flow and the nonlinear saturation process (Sipp & Lebedev 2007; Meliga 2017). The linear stability and complex dynamics of its three-dimensional counterpart, accounting for the influence of spanwise end-walls, has also been studied (Basley *et al.* 2013; Liu *et al.* 2016; Picella *et al.* 2018).

Despite its use as a representative test case for complex nonlinear dynamics in fluid mechanics, no extensive analyses of the first few bifurcations experienced by the shear-driven cavity flow has been carried out. The primary aim of the present work is to fill this gap. We have been able to determine the first primary and secondary bifurcations experienced by the flow and to draw the associated bifurcation diagram. The combined use of nonlinear direct numerical simulation, linear stability analysis and Floquet analysis then enabled us to investigate the stability of the various solution branches. More specifically, we have studied two limit cycles whose relative stability is mediated by an unstable quasiperiodic state. Our study thus complements those of Sipp & Lebedev (2007) and Meliga (2017), each of which treats one of the two limit cycles covered in this study.

A second theme of our investigation, also previously addressed by Sipp & Lebedev (2007) and Meliga (2017), is the relevance of linearization about the mean flow. For a fully developed limit cycle, nonlinear interactions contribute to the mean flow, causing a deviation from the base flow called the distortion. In this way, the mean flow inherits information from the nonlinearities (Maurel *et al.* 1995; Zielinska *et al.* 1997). From this comes the idea to linearize about the mean flow, despite the fact that the mean flow is not a solution of the stationary Navier-Stokes equations. Although the empirical use of mean flows to study nonlinear dynamics is quite old (Malkus 1956; Stuart 1958; Morris 1976), quantitative computations and comparisons are more recent, and primarily for the wake of a circular cylinder (Hammond & Redekopp 1997; Pier 2002; Barkley 2006; Mittal 2008). When successful, this procedure leads to an eigenvalue whose imaginary part reproduces very well the frequency of the periodic orbit, even quite far from its threshold. Moreover, the real part of this eigenvalue is close to zero (Barkley 2006), which would be called marginal stability if the linearization were about the base flow. This property was named RZIF (a mnemonic for Real Zero Imaginary Frequency) by Turton *et al.* (2015). An extension of RZIF, called SCM (for Self-Consistent Model) has been proposed by Mantič-Lugo *et al.* (2014, 2015), in which the mean flow is computed, not as an average of the full time-dependent flow, but precisely so that the RZIF property is satisfied, i.e. such that the mean flow is marginally stable. Neither RZIF nor SCM are always valid; counterexamples have been found for regimes in thermosolutal convection by Turton *et al.* (2015) and Bengana & Tuckerman (2018*a*). Other flows for which these properties or models have been tested are the compressible flow in the wake of a cylinder (Fani *et al.* 2018) and counter-rotating Taylor-Couette flow (Bengana & Tuckerman 2018*b*). Linearization about the mean flow has been applied to understanding the temporal spectra of turbulent flows (McKeon & Sharma 2010; Beneddine *et al.* 2016; Symon *et al.* 2018).

The paper is organized as follows: §2 introduces the configuration of the shear-driven cavity flow and the governing equations and the tools for the various analyses we have performed: linearization about the base and the mean flows, Floquet analysis, the temporal Fourier transform and the spatial Hilbert transform. Our results concerning the bifurcation scenario for this flow are presented in §3, more specifically two limit cycles produced by primary Hopf bifurcations and whose relative stability is mediated by an unstable quasiperiodic state produced by secondary bifurcations. In §4, we discuss

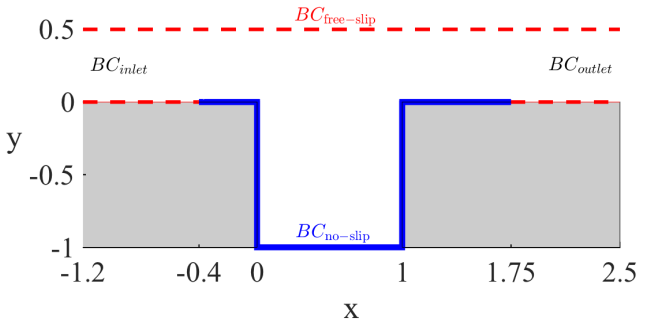

FIGURE 1. Geometry of our study. At the inlet (BC_{inlet}) a uniform unit velocity ($u = 1\ ;\ v = 0$) is imposed. Dashed red line: free-slip condition ($BC_{\text{free-slip}}$). Thick blue line: no-slip boundary condition ($BC_{\text{no-slip}}$). A free-outflow boundary condition is imposed at the outlet.

linearization about the mean flow for both limit cycles, as well as the formula of Rossiter (1964). We summarize our conclusions in §5.

2. Governing equations and numerical methods

2.1. *Problem definition*

The configuration considered is the two-dimensional incompressible viscous shear-driven flow of a Newtonian fluid over an open cavity with equal length and depth shown in figure 1. This configuration is the same as that considered by Sipp & Lebedev (2007) and Barbagallo *et al.* (2009), or more recently by Meliga (2017). We use the unperturbed upstream velocity U_∞, the cavity length L and the resulting advective time L/U_∞ to nondimensionalize the variables. The dynamics of the flow are governed by the incompressible Navier-Stokes equations

$$\begin{aligned} \frac{\partial \boldsymbol{U}}{\partial t} + \nabla \cdot (\boldsymbol{U} \otimes \boldsymbol{U}) &= -\nabla P + \frac{1}{Re}\nabla^2 \boldsymbol{U} \\ \nabla \cdot \boldsymbol{U} &= 0, \end{aligned} \tag{2.1}$$

where $\boldsymbol{U}(\boldsymbol{x}, t) = (U, V)^T$ and P are the velocity and pressure fields. The Reynolds number Re is defined as

$$Re = \frac{U_\infty L}{\nu},$$

where ν is the kinematic viscosity of the fluid. and will range between $Re = 4000$ and $Re = 5000$. The boundary conditions, illustrated in figure 1, are

$$\begin{aligned} \boldsymbol{U} &= \boldsymbol{e_x} \text{ on } \mathrm{BC}_{\text{inlet}} \\ \boldsymbol{U} &= \boldsymbol{0} \text{ on } \mathrm{BC}_{\text{no-slip}} \\ \partial_y U = V &= 0 \text{ on } \mathrm{BC}_{\text{free-slip}} \\ \partial_x \boldsymbol{U} &= \boldsymbol{0} \text{ on } \mathrm{BC}_{\text{outlet}} \end{aligned} \tag{2.2}$$

The boundary conditions at the inlet and along the wall are crucial. The flow is given a uniform profile at the inlet and develops a boundary layer structure as it advances downstream. The instability occurs where the boundary layer reaches the upstream corner of the cavity and it is the thickness of the boundary layer at this point that controls the

details of the transition. When free-slip conditions are imposed on the wall close to the inlet, then a boundary layer of an appropriate thickness develops over a shorter distance than would be the case if no-slip conditions were used over the entire wall. A shorter domain can be used, making the calculation more economical.

The Navier-Stokes equations are solved using the incompressible flow solver Nek5000 (Fischer *et al.* 2008) which is based on the spectral element method. A $\mathbb{P}_N - \mathbb{P}_{N-2}$ formulation has been used: the velocity field is discretized using N^{th} order Lagrange interpolants defined on the Gauss-Legendre-Lobatto quadrature points as basis and trial functions while the pressure field is discretized using Lagrange interpolants of degree $N-2$ defined on the Gauss-Legendre quadrature points. Finally, time integration is performed using the BDF3/EXT3 scheme: integration of the viscous term relies on backward differentiation while the convective terms are integrated explicitly using a third-order accurate extrapolation. In practice, the polynomial degree was set to $N = 6$ while the computational domain was discretized using 4000 spectral elements. The resulting mesh refinement is thus similar to that used in Sipp & Lebedev (2007).

2.2. *Base flow and linearization*

A base flow $\boldsymbol{U}_b(\boldsymbol{x})$ is a solution of the stationary Navier-Stokes equations

$$\begin{aligned} \nabla \cdot (\boldsymbol{U}_b \otimes \boldsymbol{U}_b) + \nabla P_b - \frac{1}{Re}\nabla^2 \boldsymbol{U}_b = 0 \\ \nabla \cdot \boldsymbol{U}_b = 0. \end{aligned} \tag{2.3}$$

with the boundary conditions again given by (2.2). Various techniques can be used to compute the base flow $\boldsymbol{U}_b(\boldsymbol{x})$. Because of its simplicity, the selective frequency damping (SFD) technique initially proposed by Åkervik *et al.* (2006) has been used; see also Jordi *et al.* (2014, 2015); Cunha *et al.* (2015).

Once the equilibrium $\boldsymbol{U}_b(\boldsymbol{x})$ has been computed, we determine its linear stability. To do so, we consider an infinitesimal perturbation $\boldsymbol{u}(\boldsymbol{x}, t)$ to the base flow $\boldsymbol{U}_b$, whose dynamics are governed by the linearized Navier-Stokes equations

$$\begin{aligned} \frac{\partial \boldsymbol{u}}{\partial t} + \nabla \cdot (\boldsymbol{u} \otimes \boldsymbol{U}_b + \boldsymbol{U}_b \otimes \boldsymbol{u}) = -\nabla p + \frac{1}{Re}\nabla^2 \boldsymbol{u} \\ \nabla \cdot \boldsymbol{u} = 0. \end{aligned} \tag{2.4}$$

The boundary conditions are the homogeneous version of (2.2), i.e. we now prescribe a zero velocity profile at the inlet.

$$\begin{aligned} \boldsymbol{u} = \boldsymbol{0} \text{ on } \mathrm{BC}_{\mathrm{inlet}} \\ \boldsymbol{u} = \boldsymbol{0} \text{ on } \mathrm{BC}_{\mathrm{no-slip}} \\ \partial_y u = v = 0 \text{ on } \mathrm{BC}_{\mathrm{free-slip}} \\ \partial_x \boldsymbol{u} = \boldsymbol{0} \text{ on } \mathrm{BC}_{\mathrm{outlet}} \end{aligned} \tag{2.5}$$

Solutions to (2.4) are of the form $\boldsymbol{u}(\boldsymbol{x}, t) = \hat{\boldsymbol{u}}(\boldsymbol{x}) e^{(\sigma + i\omega)t}$ + c.c., $p(\boldsymbol{x}, t) = \hat{p}(\boldsymbol{x}) e^{(\sigma+i\omega)t}$ + c.c., we obtain the eigenvalue problem

$$\begin{aligned} (\sigma + i\omega)\, \hat{\boldsymbol{u}} = \mathcal{L}_{\boldsymbol{u}_b} \hat{\boldsymbol{u}} \\ \nabla \cdot \hat{\boldsymbol{u}} = 0, \end{aligned} \tag{2.6}$$

where $\mathcal{L}_{\boldsymbol{U}_b}$ is the Jacobian of the Navier-Stokes equations linearized around $\boldsymbol{U}_b$:

$$\mathcal{L}_{\boldsymbol{U}_b} \hat{\boldsymbol{u}} \equiv \nabla \cdot (\boldsymbol{U}_b \otimes \hat{\boldsymbol{u}} + \hat{\boldsymbol{u}} \otimes \boldsymbol{U}_b) + \nabla \hat{p} - \frac{1}{Re}\nabla^2 \hat{\boldsymbol{u}} \tag{2.7}$$

The stability of the base flow is determined by the sign of the real part σ of the leading eigenvalue, which is the growth rate of the perturbation. If σ crosses zero for an eigenvalue with non-zero imaginary part ω, then a Hopf bifurcation leads to a limit cycle whose frequency at onset is ω. In our case, the base flow undergoes a first Hopf bifurcation at $Re_2 = 4126$, leading to a limit cycle LC_2 and a second Hopf bifurcation at $Re_3 = 4348$ gives rise to LC_3.

We computed the leading eigenvalues and eigenvectors using a time-stepper approach; see, e.g., Edwards *et al.* (1994). Our stability calculation typically used a Krylov subspace of dimension $K = 256$ and a sampling period $\Delta T = 10^{-3}$ non-dimensional time units. Eigenvalues were considered to be converged if the residual obtained from the Arnoldi decomposition was below 10^{-6}.

2.3. *Mean flow and linearization*

At the threshold of a Hopf bifurcation, linearization about the base flow leads to an eigenvalue whose real part is zero and whose imaginary part is the frequency of the limit cycle which is produced. As the Reynolds number is increased and the limit cycle develops nonlinearly and deviates from the base flow, eigenvalues obtained by linearization about the base flow no longer correspond to the properties of the limit cycle. However, linearization about the mean flow often leads to an eigenvalue whose imaginary part is closer to the nonlinear frequency.

We consider a Reynolds decomposition of the instantaneous flow field, i.e.

$$\boldsymbol{U}(\boldsymbol{x},t) = \overline{\boldsymbol{U}}(\boldsymbol{x}) + \boldsymbol{u}(\boldsymbol{x},t)$$

where $\overline{\boldsymbol{U}}(\boldsymbol{x})$ is the mean flow and $\boldsymbol{u}(\boldsymbol{x},t)$ is the zero-mean fluctuation. Introducing this decomposition into the Navier-Stokes equations and averaging shows that $\overline{\boldsymbol{U}}$ is governed by the Reynolds Averaged Navier-Stokes (RANS) equations

$$\begin{aligned} \nabla\cdot\left(\overline{\boldsymbol{U}}\otimes\overline{\boldsymbol{U}}\right) + \nabla\overline{P} - \frac{1}{Re}\nabla^2\overline{\boldsymbol{U}} &= -\nabla\cdot\left(\overline{\boldsymbol{u}\otimes\boldsymbol{u}}\right) \\ \nabla\cdot\overline{\boldsymbol{U}} &= 0 \end{aligned} \tag{2.8}$$

with boundary conditions (2.2). The presence of the Reynolds stress tensor $\overline{\boldsymbol{u}\otimes\boldsymbol{u}}$ of the fluctuation means that these equations are not closed. We compute the mean flow $\overline{\boldsymbol{U}}(\boldsymbol{x})$ of a period-T limit cycle by carrying out a full nonlinear simulation via (2.1) and time-averaging:

$$\overline{\boldsymbol{U}}(\boldsymbol{x}) = \frac{1}{T}\int_0^T \boldsymbol{U}(\boldsymbol{x},t)\ \mathrm{d}t.$$

The equations governing the dynamics of the fluctuation $\boldsymbol{u}(\boldsymbol{x},t)$, obtained by subtracting (2.8) from (2.1), are

$$\begin{aligned} \frac{\partial\boldsymbol{u}}{\partial t} + \nabla\cdot\left(\boldsymbol{u}\otimes\overline{\boldsymbol{U}} + \overline{\boldsymbol{U}}\otimes\boldsymbol{u}\right) &= -\nabla p + \frac{1}{Re}\nabla^2\boldsymbol{u} - \nabla\cdot\left(\boldsymbol{u}\otimes\boldsymbol{u} + \overline{\boldsymbol{u}\otimes\boldsymbol{u}}\right) \\ \nabla\cdot\boldsymbol{u} &= 0. \end{aligned} \tag{2.9}$$

with homogeneous boundary conditions (2.5). The equations differ from the linearized Navier-Stokes equations by the presence of the last two terms in the right-hand side. The first term, $\nabla\cdot(\boldsymbol{u}\otimes\boldsymbol{u})$, is the usual quadratic interaction term neglected in base flow linear stability analyses. The second term, $\nabla\cdot(\overline{\boldsymbol{u}\otimes\boldsymbol{u}})$ is the divergence of the Reynolds stress tensor of the fluctuation.

Recent studies focusing on mean flow stability analyses discard these two terms, leading

to the linearized equations

$$\begin{aligned} \frac{\partial \boldsymbol{u}}{\partial t} + \nabla \cdot \left(\boldsymbol{u} \otimes \overline{\boldsymbol{U}} + \overline{\boldsymbol{U}} \otimes \boldsymbol{u} \right) &= -\nabla p + \frac{1}{Re} \nabla^2 \boldsymbol{u} \\ \nabla \cdot \boldsymbol{u} &= 0. \end{aligned} \tag{2.10}$$

Using once again a normal mode ansatz, this set of equations is reduced to the eigenvalue problem

$$\begin{aligned} (\sigma + i\omega)\, \hat{\boldsymbol{u}} &= \mathcal{L}_{\overline{\boldsymbol{U}}} \hat{\boldsymbol{u}} \\ \nabla \cdot \hat{\boldsymbol{U}} &= 0, \end{aligned} \tag{2.11}$$

where $\mathcal{L}_{\overline{\boldsymbol{U}}}$ is now the Navier-Stokes operator linearized around the mean flow, with $\overline{\boldsymbol{U}}$ substituted for $\boldsymbol{U}_b$ in (2.7).

Although the mean flow is not an equilibrium solution of the Navier-Stokes solution, this approach has proved unexpectedly successful in characterizing the frequencies of the full nonlinear solutions of the Navier-Stokes equations (Barkley 2006; Mittal 2008; Mantič-Lugo *et al.* 2014, 2015; Turton *et al.* 2015; Meliga *et al.* 2016). For a counter-example, however, see Turton *et al.* (2015). Various theoretical justifications for dropping or modeling the extra two terms in the right-hand side of (2.9) have been proposed, such as:

(i) The quadratic interaction of the fluctuation with itself as well as its temporal mean are small enough so that they can both be neglected.

(ii) The instantaneous Reynolds stress tensor $\boldsymbol{u} \otimes \boldsymbol{u}$ is approximately equal to its temporal average $\overline{\boldsymbol{u} \otimes \boldsymbol{u}}$ so that they cancel out.

(iii) The functional form of these terms and their interaction with the linear operator $\mathcal{L}_{\overline{\boldsymbol{u}}}$ and with the frequency ω are such that they have little effect.

(iv) The resolvent operator $(i\omega - \mathcal{L})^{-1}$ is sharply peaked or of low rank.

These crucial questions are discussed in, e.g. Barkley (2006); Sipp & Lebedev (2007); McKeon & Sharma (2010); Mantič-Lugo *et al.* (2014, 2015); Turton *et al.* (2015); Beneddine *et al.* (2016); Symon *et al.* (2018).

2.4. *Floquet analysis*

Our study of the shear-driven cavity focuses on two limit cycles, denoted by LC_2 and LC_3, created by primary Hopf bifurcations and destabilized via secondary bifurcations. Floquet analysis will be used to characterize this destabilization. The dynamics of an infinitesimal perturbation $\boldsymbol{u}(\boldsymbol{x}, t)$ evolving in the vicinity of a T-periodic limit cycle $\boldsymbol{U}(\boldsymbol{x}, t)$ are governed by the linearized Navier-Stokes equations

$$\begin{aligned} \frac{\partial \boldsymbol{u}}{\partial t} &= \mathcal{L}_{\boldsymbol{U}(t)} \boldsymbol{u} \\ \nabla \cdot \boldsymbol{u} &= 0 \end{aligned} \tag{2.12}$$

with homogeneous boundary conditions (2.5). This set of equations is non-autonomous, as the operator $\mathcal{L}_{\boldsymbol{U}(t)}$ is T-periodic. Solutions to Eq. (2.12) are of the Floquet form

$$\boldsymbol{u}(\boldsymbol{x}, t) = \hat{\boldsymbol{u}}(\boldsymbol{x}, t) e^{(\sigma_F + i\omega_F)t} + \text{c.c.}$$

where $\hat{\boldsymbol{u}}(\boldsymbol{x}, t)$ are the T-periodic Floquet modes and $(\sigma_F + i\omega_F)$ the Floquet exponents. The stability is determined by the Floquet multipliers

$$\mu = e^{(\sigma_F + i\omega_F)T}.$$

If the moduli of the Floquet multipliers are smaller than one, perturbations will decay exponentially fast and the orbit is stable. On the other hand, if at least one of the

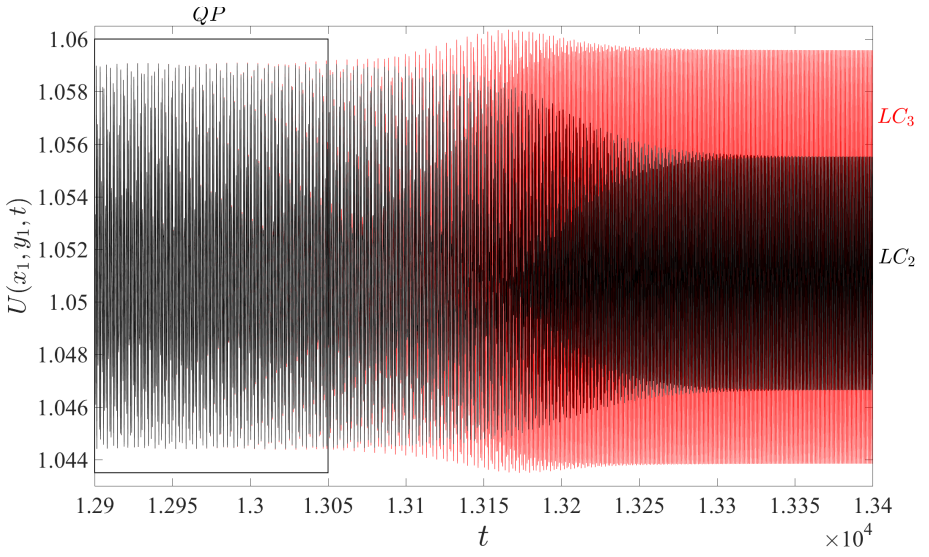

FIGURE 2. Time traces of streamwise velocity at $Re = 4460$ for two simulations. The initial condition of the simulation is (2.13). For $\alpha = 0.47562027$ the system evolves towards LC_2, shown as the black curve. For $\alpha = 0.47562256$ it evolves towards LC_3, shown as the higher-amplitude red curve.

Floquet multipliers has a modulus greater than one, then that perturbation will grow exponentially and the orbit is unstable; see, e.g. Barkley & Henderson (1996) and Gioria *et al.* (2009). In our study the Floquet exponents are complex and the imaginary part ω_F of the Floquet exponent is the argument (angle) of the Floquet multiplier. The presence of an imaginary part leads to quasiperiodic behavior. More details and results are shown in §3.4.

2.5. *Edge state technique for computing the unstable quasiperiodic state*

As will be shown in §3, there is a range of Reynolds numbers over which limit cycles LC_2 and LC_3 co-exist. In phase space, on the boundary between the basins of attraction of these limit cycles, is an unstable quasi-periodic state QP. (More specifically, QP is an edge state, meaning that within the boundary, trajectories are attracted to it.) In order to compute QP, we use the same technique as in Itano & Toh (2001) or Duguet *et al.* (2008) for the laminar-turbulent edge state. In such cases, whether a trajectory evolves towards a turbulent or laminar state depends on the initial condition. Some initial conditions evolve directly to turbulence, others decay directly to the laminar state. By appropriately weighting turbulent and laminar solutions, an initial condition can be constructed so that the resulting trajectory remains a long time on the edge state before diverging towards one of these two attractors.

In our problem, a quasi-periodic state separates the two stable limit cycles LC_2 and LC_3. Therefore we construct a weighted sum of the two, seeking an initial condition $\boldsymbol{U}(\boldsymbol{x}, 0)$ that will take as long as possible to converge to either limit cycle. Using the same bisection technique as in Lopez *et al.* (2017), this initial condition is given by

$$\boldsymbol{U}(\boldsymbol{x}, t) = \alpha \boldsymbol{U}_{LC_2} + (1 - \alpha)\boldsymbol{U}_{LC_3}. \tag{2.13}$$

For $\alpha = 1$, the initial condition is LC_2 and for $\alpha = 0$, it is LC_3. For each Reynolds number considered, we successively delimit an interval of α by bisection to capture the quasi-

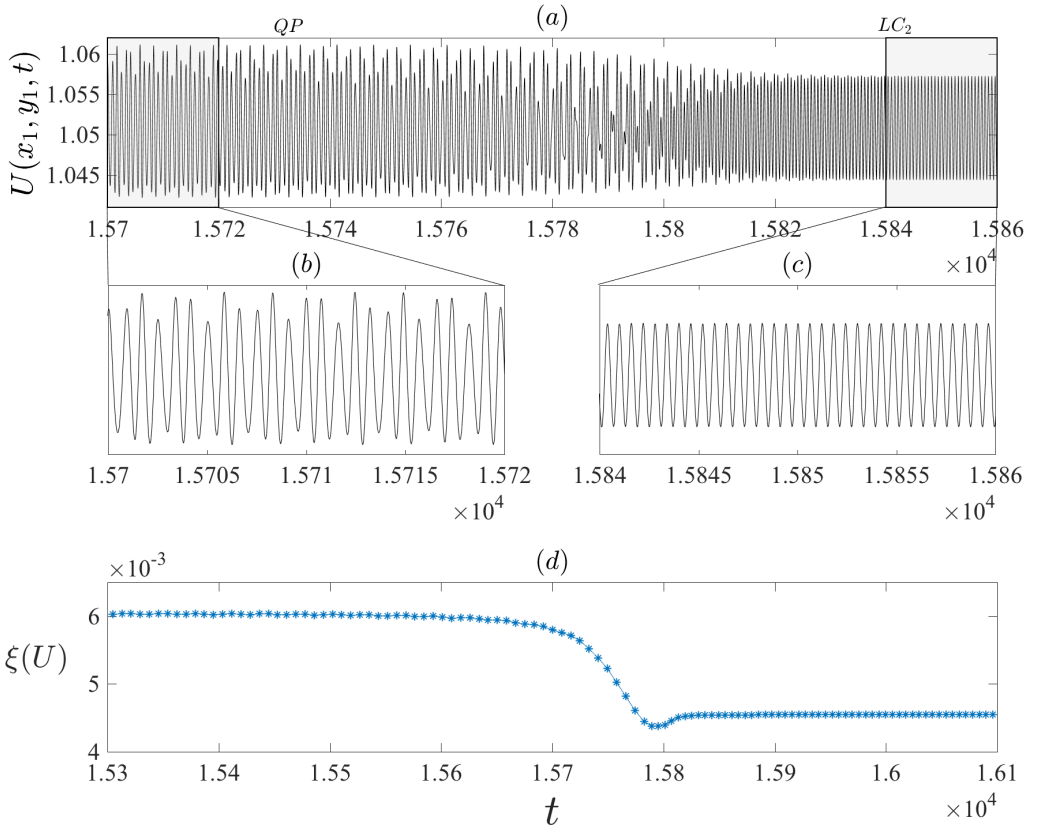

FIGURE 3. (a) Time series of streamwise velocity at $(x_1, y_1) = (1.2, 0.2)$ and $Re = 4580$ for a simulation with $\alpha = 0.829630407714844$. The regimes corresponding to QP and to LC_3 are shown in (b-c). (d) The standard deviation is computed by a sliding window.

periodic state. As an illustration, we plot in figure 2 the time evolution of streamwise velocity recorded by a probe located at $(x_1, y_1) = (1.2, 0.2)$ for $\alpha = 0.47562027$ and 0.47562256. A slight difference in α will bring the system after a long transient regime to either LC_2 or LC_3.

2.6. *Standard deviation*

To construct the bifurcation diagram, we seek an appropriate measure of the oscillation amplitude as a function of Re. Time series from limit cycles LC_2 and LC_3 are shown in figures 2 and 3(c). Their amplitudes are easily obtained by measuring the maxima in a time series or the fundamental peak in the temporal Fourier spectrum. In contrast to these, which have maxima of constant amplitudes, the quasiperiodic state existing in the overlap region has maxima of varying heights as shown in figure 2 and in 3(b). To extract a single amplitude in their study of the cubic lid-driven cavity, Lopez *et al.* (2017) used the standard deviation from the mean flow, defined as

$$\xi(U) = \left[\frac{1}{N} \sum_{n=0}^{N} \left(U(x_1, y_1, t_n) - \overline{U}(x_1, y_1) \right)^2 \right]^{1/2} \tag{2.14}$$

with $U(x_1, y_1, t_n)$ the streamwise velocity measured at $(x_1, y_1) = (1.2, 0.2)$ and at each instant t_n, N the number of measurements in the time series, and $\overline{U}(x_1, y_1)$ the temporal

mean. We used the edge state technique described in §(2.5) to compute a time series in which the QP is maintained for a long time. In figure 3(d), we show the standard deviation of the time series plotted in figure 3(a). The standard deviation is computed over all times of a sliding window containing fifty peaks. Once the deviation is computed, the window is shifted by ten peaks and we compute the deviation again over fifty peaks. Figure 3(d) shows two regimes of constant $\xi(U)$ corresponding to QP and LC_2, justifying the choice of $\xi(U)$ for the bifurcation diagram.

2.7. *Hilbert transform*

We use the Hilbert transform to obtain spatial characteristics of the vortex shedding. The Hilbert transform constructs a complex analytic signal $f_a(x)$ from real data $f(x)$. In contrast to a real signal that has negative and positive frequencies, this analytic signal is complex and has only positive frequencies. This signal is obtained by

$$f_a(x) = f(x) + i\mathcal{H}(f(x)) \tag{2.15}$$

The imaginary part $\mathcal{H}(f(x))$ is its Hilbert transform defined by phase shifting the positive and negative frequencies of the original real signal by $-\pi/2$ and $\pi/2$ respectively. More details about the Hilbert transform can be found in Smith (2007). Equation (2.15) is written in polar form

$$f_a(x) = A(x)e^{i\Phi(x)} \tag{2.16}$$

Thus we can extract the envelope (amplitude $A(x)$) and the phase $\Phi(x)$ from the analytic signal at each location, which is the main interest in using the Hilbert transform. We present the results in detail in textsection 3.3.

3. Bifurcation scenario

3.1. *Overview*

The flow over a shear-driven cavity at low Reynolds number consists of a free laminar shear layer and one large recirculation within the cavity. As we increase the Reynolds number, the mixing layer is fed by the shear stress and its thickness develops over the cavity. As widely presented in several studies (Rockwell & Naudascher 1978), it is common to observe self-sustained oscillations in such configurations, in which the flow impacts on a wall. In figure 4(a) we show the bifurcation diagram over the range of Reynolds number $Re \in [4000, 5000]$. We represent the standard deviation from the mean of the streamwise velocity at a point as described in §2.6. The standard deviation is computed over all times t_n of the time series corresponding to LC_2, LC_3 or QP. The line $\xi(U) = 0$ represents the solution of the stationary Navier-Stokes equations (base flow). We plot the stable and unstable states with bold and dashed curves respectively. The base flow is stable for $Re < Re_2$ where $Re_2 \approx 4126$ is the critical Reynolds number of the first Hopf bifurcation. This threshold is obtained by quadratic interpolation of amplitudes and differs by only 0.34% from that found by Sipp & Lebedev (2007). Above this threshold, the base solution exists but is unstable. We observe a second Hopf bifurcation at $Re_3 \approx 4348$, also from quadratic interpolation of amplitudes, which agrees with the threshold measured by Meliga (2017), differing only by 0.005%. These successive Hopf bifurcations lead after saturation by nonlinear interactions to two limit cycles which we name LC_2 and LC_3 because they display two or three pairs of counter-rotating vortices respectively, as will be shown in the next section. Figure 4(b) shows the schematic phase portrait corresponding to the bifurcation diagram. The stable base flow *(i)* loses its stability through a primary Hopf bifurcation *(ii)* at Re_2 producing the limit cycle LC_2. *(iii)*

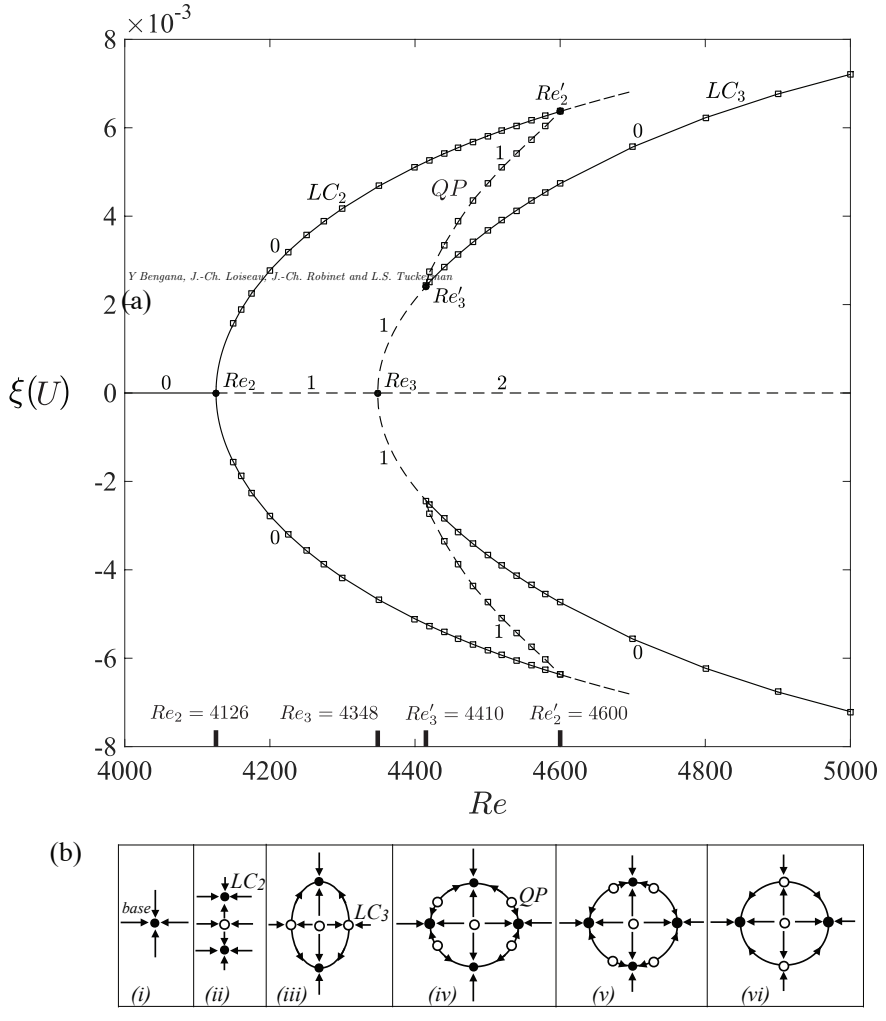

FIGURE 4. (a) Bifurcation diagram of the shear-driven cavity flow for $Re \in [4000, 5000]$. On the x-axis, we show the Reynolds number Re and on the y-axis the standard deviation from the mean of the streamwise velocity at one point. The bold dots on the curves and the thick ticks on the x-axis show the critical Reynolds numbers. The integers show the number of unstable directions (counting a complex conjugate pair as a single direction). We represent stable states by bold curves and unstable ones by dashed curves. The line $\xi(U) = 0$ indicates the stationary base flow. The first Hopf bifurcation occurs at $Re_2 \approx 4126$ and the second at $Re_3 \approx 4348$. These two thresholds have been calculated by a quadratic interpolation from the amplitudes. The Hopf bifurcations give rise to limit cycles LC_2 and LC_3. LC_2 is stable from its threshold until $Re'_2 \approx 4600$ where it loses stability to LC_3. LC_3 is unstable from Re_3 to $Re'_3 \approx 4410$ and above this Reynolds number it becomes stable. Between LC_2 and LC_3 in the overlap region $Re \in [4400, 4600]$ there exists a quasiperiodic state QP, which has been computed by using $\alpha LC_2 + (1 - \alpha)LC_3$ as an initial condition for the full nonlinear simulation where $\alpha = \alpha(Re)$. (b) From left to right, the schematic phase portraits corresponding to the bifurcation diagram. The ordinate and abcissa can be considered to be projections onto the eigenmodes leading to LC_2 and LC_3, respectively. The black dots and hollow circles show the stable and unstable states. *(i)* Stable base flow. *(ii)* Limit cycle LC_2 is shown as bifurcating in the vertical direction. *(iii)* LC_3 bifurcates in the horizontal direction. *(iv,v)* The circle moving on the orbit indicates the quasiperiodic state QP. *(vi)* QP has disappeared, stabilizing LC_3.

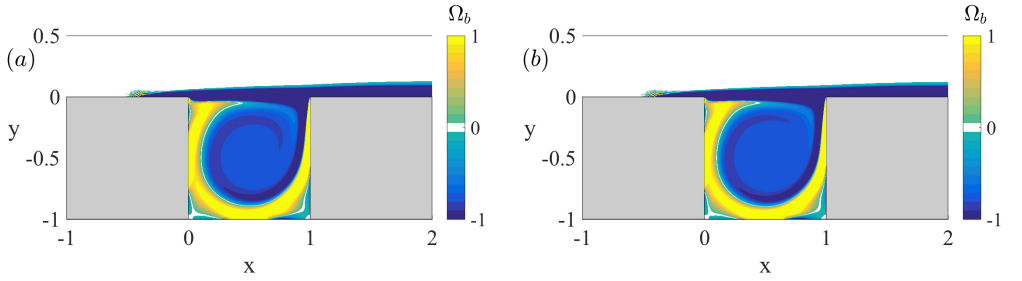

FIGURE 5. Stationary solution (base flow). We show the vorticity Ω_b for (a) $Re = 4500$ and (b) $Re = 5000$. The change in the base flow with Reynolds number is not visible in this representation.

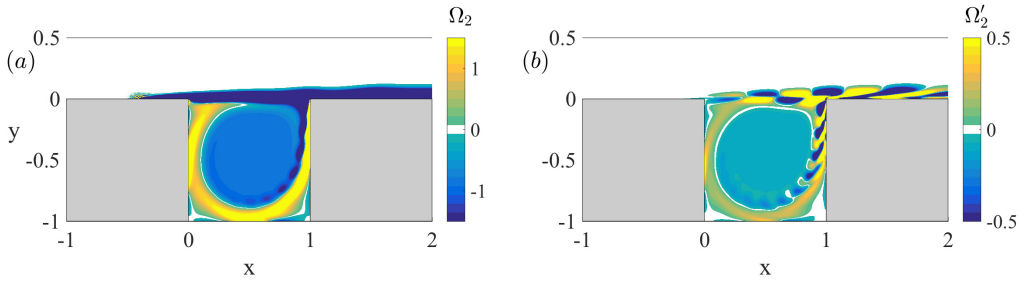

FIGURE 6. (a) Vorticity Ω and (b) distortion ($\Omega' = \Omega - \bar{\Omega}$) for LC_2 at $Re = 4500$.

Another primary Hopf bifurcation at Re_3 produces the limit cycle LC_3. *(iv)* A secondary subcritical Hopf bifurcation from LC_3 at Re_3' produces the quasiperiodic state QP, which moves *(v)* in phase space towards LC_2 until it undergoes another secondary subcritical Hopf bifurcation *(vi)* at Re_2' which destroys QP and destabilizes LC_2. Above Re_3', LC_3 is stable at least until $Re = 5000$. Another Hopf bifurcation and interesting dynamics occur above $Re = 5000$ but these will not be discussed in this paper.

The base flow is shown in figure 5 for $Re = 4500$ and $Re = 5000$. The change in the mixing layer when we increase Re is not qualitatively visible, although the Reynolds number plays a key role in the mixing layer instability. Instantaneous visualizations of LC_2 are shown in Figure 6. Figure 6(a) shows that the vorticity is dominated by the mean flow, which makes the structures difficult to detect. Subtracting the mean flow from the vorticity we obtain the fluctuations shown in figure 6(b). Although the structures are quite visible, the presence of two superposed rows of vorticity deviations of opposite sign is misleading, since the vorticity itself has only one such row. (The different appearance of the vorticity and vorticity deviation is a consequence of the dominance of the vorticity of the base flow.) For this reason, we will represent fields by their vertical velocity fluctuations when we want to show structures, since the vertical velocity of the base flow does not dominate that of the other regimes.

In figures 7 and 8 we show the instantaneous vertical velocity fluctuations for LC_2 and LC_3 over one period. We observe four organized structures, i.e. two pairs of counter-rotating vortices, in LC_2 and six organized structures, i.e. three pairs of counter-rotating vortices, for LC_3. The behavior resembles that of traveling waves. The structures progress steadily to the right but the overall amplitude is not uniform. In these figures, structures of opposite sign are produced by a feedback mechanism. At the downstream corner, the structures split, as reported by Rockwell & Knisely (1980): one part follows the fluid

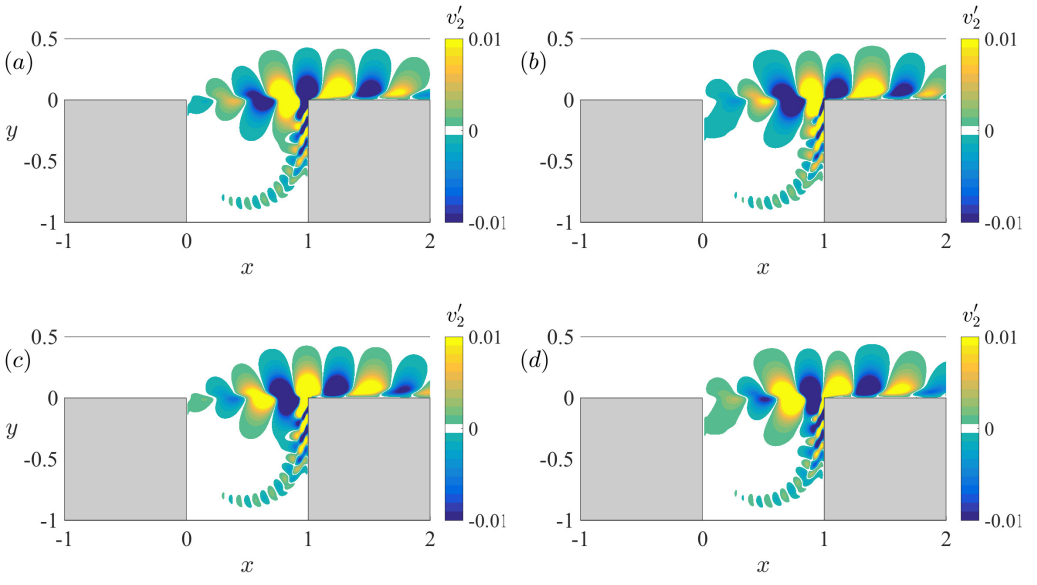

FIGURE 7. Instantaneous vertical velocity fluctuations ($V' = V - \bar{V}$) for LC_2 over one period for $Re = 4500$. (a) t = 0 (b) $T/4$ (c) $T/2$ (d) $3T/4$. The structures are advected downstream, as they would be for a traveling wave. In the range of the cavity $x \in [0, 1]$ we count two pairs of counter-rotating vortices. The vortices are deformed downstream for $x > 1.2$, due to the change to a free-slip boundary condition.

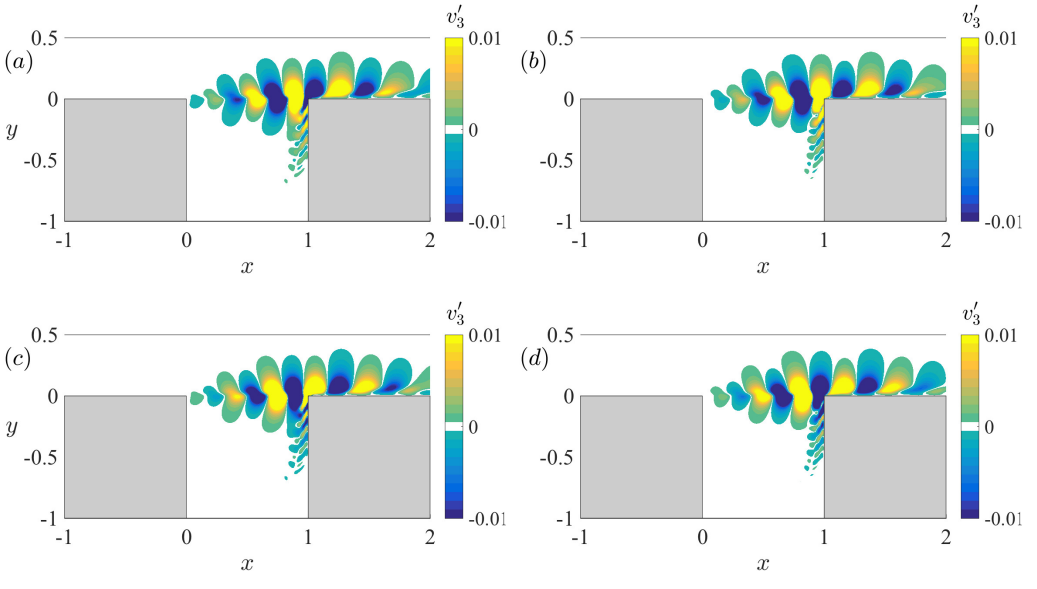

FIGURE 8. Instantaneous vertical velocity fluctuations ($V' = V - V_m$) for LC_3 over one period for $Re = 4500$. (a) t = 0 (b) $T/4$ (c) $T/2$ (d) $3T/4$. We observe the same dynamics as in LC_2 shown in figure 7. Over the range $x \in [0, 1]$ we count three pairs of counter-rotating vortices.

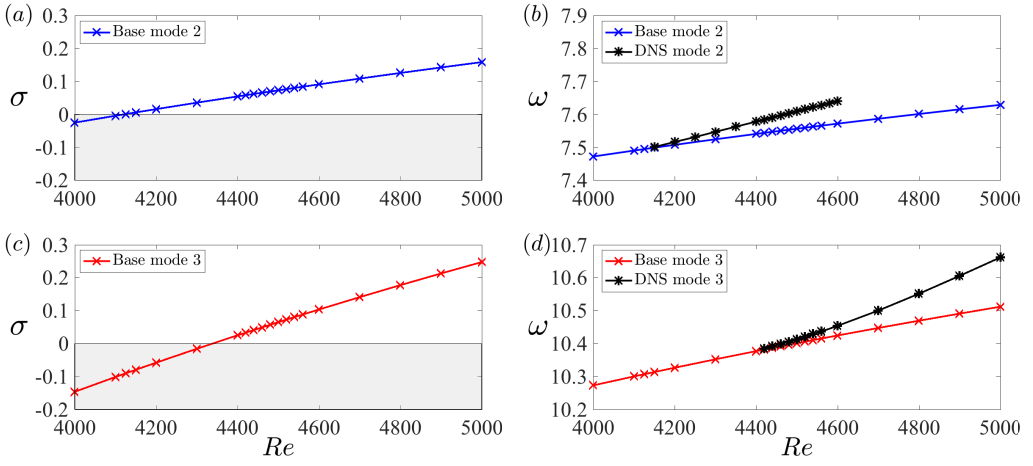

FIGURE 9. Eigenvalues $\sigma+i\omega$ from linear stability analysis about the base solution with blue and red crosses, and nonlinear frequency from DNS simulation with black stars. (a,c): Growth rate σ of the most unstable eigenmode. In this range of Reynolds number, are two successive Hopf bifurcations as shown in the bifurcation diagram of figure 4. The growth rates for eigenvalues leading to LC_2 and LC_3 are shown with blue and red stars respectively. (b,d): Frequency ω of linear stability analysis about the base state and nonlinear simulation. The nonlinear and linear frequencies agree at onset, but when we increase the Reynolds number the nonlinear frequency deviates from that resulting from linear stability about the base flow.

downstream, while the other is entrained by the cavity recirculation and returns to feed the flow at the upstream corner, sustaining the vortex generation. The mechanism behind the oscillations is the same for both limit cycles LC_2 and LC_3. The temporal frequency is near 7 for LC_2 and near 10 for LC_3. These modes are selected by the cavity length and the mean velocity of the mixing layer as described by Rossiter (1964) and as will be discussed in §4.3.

3.2. *Linearization about the base flow*

In figure 9 we present the results of linear stability analysis about the base flow. We plot the growth rates σ in figure 9(a,c) and the frequencies ω in figure 9(b,d). As previously stated, two successive Hopf bifurcations correspond to two different modes. We plot in (a,b) the eigenvalue leading to LC_2 and (c,d) that corresponding to LC_3. The zero crossing of the growth rate marks the Hopf bifurcation at which that base flow becomes unstable. As presented in the bifurcation diagram in figure 4, the base flow acquires a first unstable direction at around $Re_2 \approx 4126$ and a second unstable direction at $Re_3 \approx 4348$. Figure 9(b,d) also shows the nonlinear frequencies for the two limit cycles. These agree with the eigenfrequencies at Re_2 and Re_3, as is necessarily the case for a supercritical bifurcation, but as the Reynolds number increases, the frequencies diverge from one another. Indeed linear stability analysis is valid only for small deviations from the base flow: the frequency extracted at an early stage of a nonlinear simulation initialized by a small perturbation from the base flow will be equal to that given by linear analysis, but the nonlinear interactions will cause it to evolve with time to the nonlinear frequency (Barkley 2006; Mantič-Lugo *et al.* 2014, 2015; Meliga *et al.* 2016).

Figure 10 shows a portion of the eigenvalue spectra for $Re = 4200$, 4500, and 5000. We show in blue circles the eigenvalues that satisfied the convergence tolerance of 10^{-6} and in red stars those that did not converge. The first eigenvalue has crossed the $\sigma = 0$

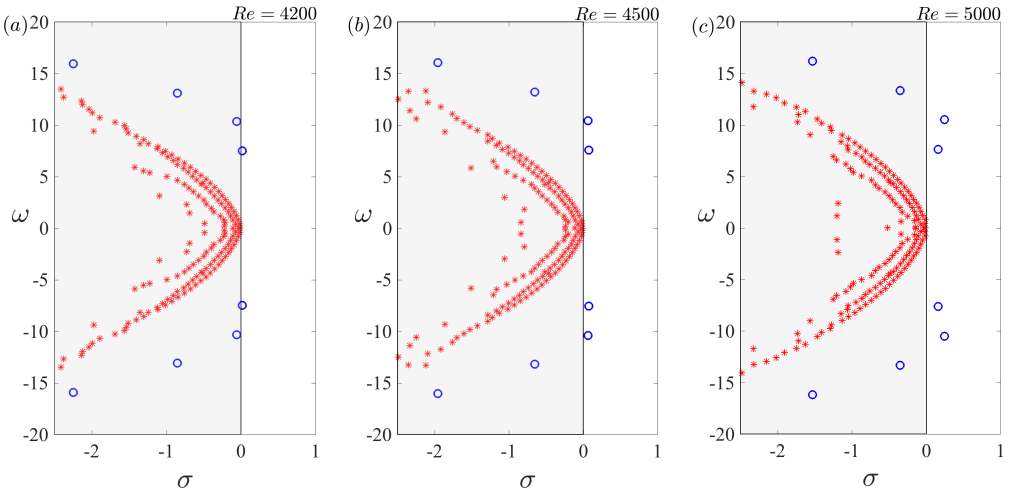

FIGURE 10. Spectra of complex-conjugate eigenvalues of the base flow for (a) $Re = 4200$, (b) $Re = 4500$, (c) $Re = 5000$. Blue circles designate the converged eigenvalues and red stars the eigenvalues that did not converge. In these figures we observe the evolution of modes leading to LC_2 and LC_3. The third converged mode, which is stable in this range of Reynolds number, crosses the imaginary axis for $Re \approx 6000$ (not shown).

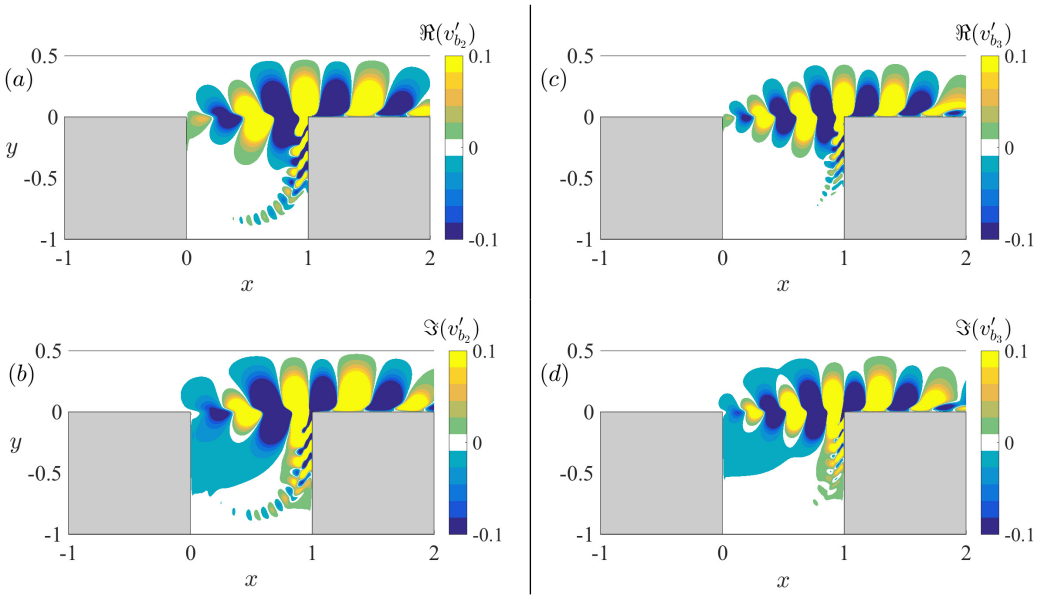

FIGURE 11. Vertical velocity of the real and imaginary parts of the leading unstable eigenmodes about the base flow at $Re = 4500$. (a,b) LC_2 and (c,d) LC_3.

axis by $Re = 4200$ and the second eigenvalue has crossed by $Re = 4500$. At this Re there are two unstable eigenvalues with almost the same growth rate. At $Re = 5000$ these two unstable eigenvalues have further increased and a third stable mode approaches the imaginary axis, becoming unstable at $Re \approx 6000$ (not shown).

Figure 11(a,b) shows the real and imaginary parts of the eigenvector of LC_2 and figure

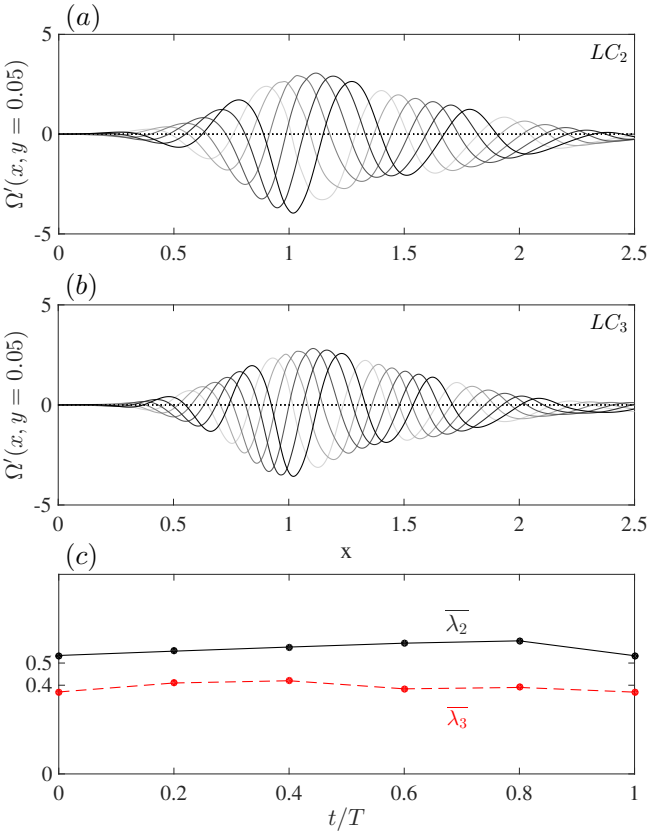

FIGURE 12. Vorticity fluctuations above the cavity $\Omega'(x, y = 0.05)$ over one period. We observe the behavior of a traveling wave for (a) LC_2 and (b) LC_3. Because the wavelength evolves in space, we calculate the average wavelength $\overline{\lambda}$ as shown in figure (c), in solid and dashed line for LC_2 and LC_3 respectively. The mean wavelength is near 0.5 for LC_2 and near 0.4 for LC_3.

11(b,d) shows the eigenvector of LC_3. The phase is shifted by a quarter wavelength between the real and imaginary parts for both eigenvectors, typical of quasi-traveling wave behavior. We observe two pairs of counter-rotating vortices on LC_2 and three on LC_3, as was mentioned in the discussion of figures 7 and 8.

3.3. *Spatial analysis and Hilbert transform*

We have shown in the previous sections that LC_2 and LC_3 have different numbers of vortices. figure 12(a,b) shows the vorticity fluctuations Ω' slightly above the cavity at $y = 0.05$ and for $x \in [0, 2.5]$ for these limit cycles. Curves from light to dark show the vorticity fluctuations at various phases of the temporal period. These two figures show qualitatively the behavior of a traveling wave, but quantitatively the wavelength and amplitude are not constant. For this reason, at a fixed time, i.e for each curve shown in figure 12(a,b) we compute an average wavelength $\overline{\lambda}$. Averaging the wavelength over only $x \in [0, 1]$ is not possible because this range contains too few wavelengths. Figure 12(c) shows $\overline{\lambda}$ as the dashed and solid curves for LC_3 and LC_2. The wavelengths vary little over time and have temporal averages $\langle\overline{\lambda_2}\rangle = 0.56$ and $\langle\overline{\lambda_3}\rangle = 0.39$.

We use the Hilbert transform presented in §2.7 to analyse in detail the final curve $\Omega'(x, y = 0.05)$ showns in figure 12a,b. We recall that the Hilbert transform produces

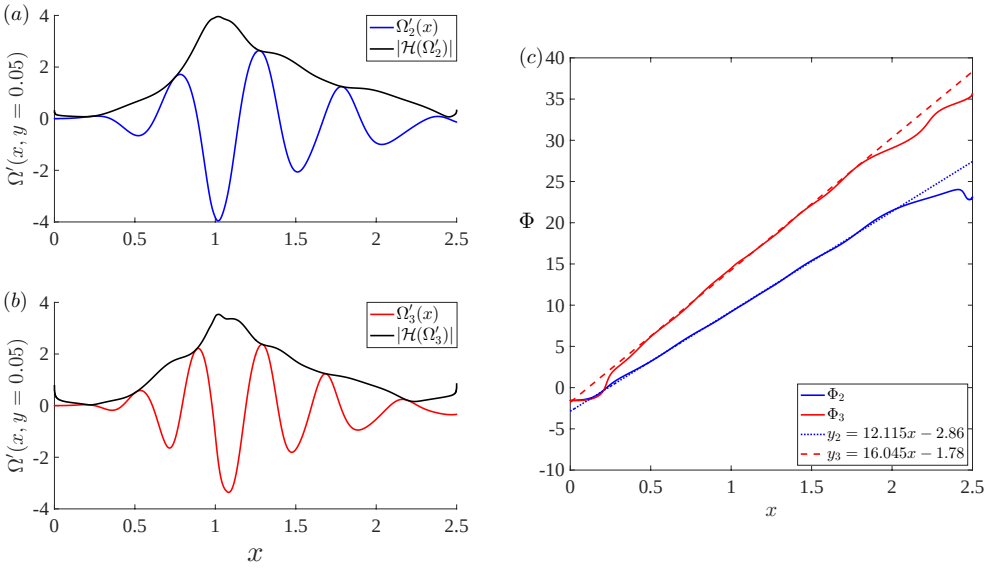

FIGURE 13. Hilbert transform of vorticity fluctuations $\Omega'(x, y = 0.05)$. (a,b): vorticity fluctuation, its spline interpolation and the modulus of the Hilbert transform, which is the envelope of the signal. (c): The ratio between the real and imaginary parts of the Hilbert transform is the phase whose evolution is shown for LC_3 (red) and for LC_2 (blue). Linear fits to the phases Φ_i are shown by dashed and dotted curves

from a real signal $f(x)$ a complex signal $f_a(x)$ which is written in polar form as $A(x)e^{i\Phi(x)}$. We show in figure 13(a,b) the vorticity fluctuations $\Omega'_2(x)$ and $\Omega'_3(x)$ for LC_2 and LC_3 with black curves. Over the range $x \in [0.5, 2.3]$, there are two influential locations: one is the impact of the vortices on the downstream corner and the second is the change of boundary condition from no-slip to free-slip. Because the Hilbert transform is very sensitive, we have interpolated the signals by a cubic spline. The figure also shows the amplitudes $A(x)$ of the Hilbert transform of the signals. These show a maximum at the downstream corner, the location of impact of the vortices on the vertical wall at $x = 1$. Figure 13(c) shows the phase $\Phi(x)$ for LC_2 and LC_3. The slope of $\Phi(t)$ is the wavenumber k. We show with dashed and dotted lines the linear regression calculated over $x \in [0.5, 1.5]$. The wavenumber for LC_2 obtained in this way is $k = 12.115$ and that for LC_3 is $k = 16.045$, leading to wavelengths $\lambda_2 = 0.519$ and $\lambda_3 = 0.392$. These values are fairly close to the values $\langle\overline{\lambda}_2\rangle = 0.56$ and $\langle\overline{\lambda}_3\rangle = 0.39$ obtained by measuring wavelengths, as shown in figure 12. The value $\lambda_2 \approx 0.5$ justifies our designation of LC_2 as containing two pairs of vortices, since $L/\lambda_2 \approx 2$, but the value $\lambda_3 \approx 0.4$ leads to $L/\lambda_3 \approx 2.5$ rather than 3.

3.4. *Quasiperiodic state and Floquet analysis*

As presented in the previous sections, there is a range of Re over which two limit cycles coexist, separated by a quasiperiodic state. We mention here that this state is probably periodic rather than strictly quasiperiodic, because of the well-known nonlinear phenomenon of frequency locking, but its effective period is very long and we will continue to consider it to be quasiperiodic. Figures 2 and 3(b) show the time series corresponding to the quasiperiodic state. Figure 14 presents temporal Fourier spectra for three values of Re of the quasiperiodic state, which has two fundamental frequencies close to ω_2 and

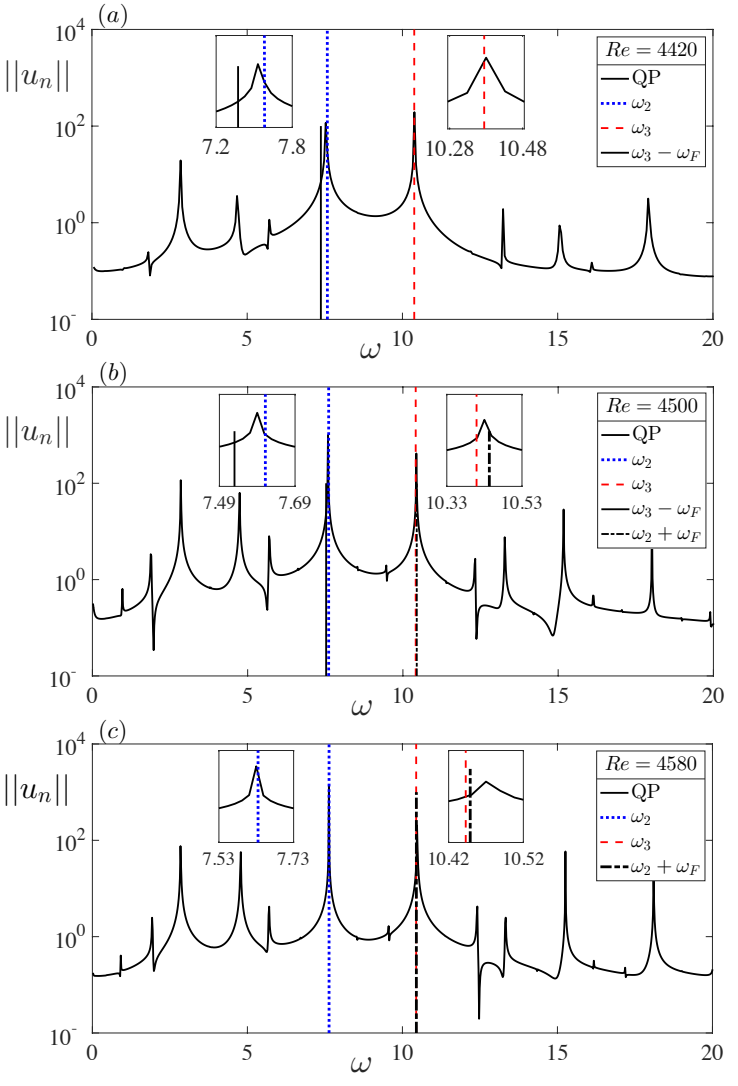

FIGURE 14. Temporal Fourier spectra of the quasiperiodic state (black bold curves), computed with the edge state technique at (a) $Re = 4420$, near Re'_3, (b) $Re = 4500$ and (c) $Re = 4580$, near Re'_2. The vertical lines show the frequencies ω_2 (blue dotted lines) and ω_3 (red dashed lines) of LC_2 and LC_3 at the corresponding values of Re. (a) Near Re'_3 where QP is near LC_3, the peak ω_{QP_3} of the QP spectrum matches its analogue ω_3 (red dashed line) on LC_3, while ω_{QP_2} is slightly to the left of ω_2 (blue dotted line) of LC_2. (c) Near Re'_2, where QP is near LC_2, the peak of ω_{QP_2} of the QP spectrum matches its analogue ω_2 (blue dotted line), while ω_{QP_3} is to the right of ω_3 (red dashed line) from LC_3. (b) Away from Re'_2 and Re'_3, both frequencies ω_{QP_2} and ω_{QP_3} are shifted slightly from their analogues on LC_2 and LC_3. The vertical bold and dash-dotted lines show the frequencies calculated by Floquet analysis about LC_2 by $\omega = \omega_2 + \omega_F$ (dash-dotted line) and about LC_3 by $\omega = \omega_3 - \omega_F$ (bold line). Near the thresholds at (a) $Re = 4420$ and (c) $Re = 4580$, the frequency obtained by Floquet analysis about LC_3 and LC_2 are very close to ω_{QP_2} and ω_{QP_3}. At $Re = 4500$ in figure (b) the frequencies obtained by Floquet analysis about LC_2 and LC_3 are also close to their analogues in the quasiperiodic state even though the linear analysis is only valid at the vicinity of the thresholds.

ω_3 as shown by the dotted and dashed lines in figures 14(a-c). QP can be viewed as a nonlinear superposition of LC_2 and LC_3

$$\boldsymbol{U}_{\mathrm{QP}}(x,y,t) = \sum_n \sum_m c_{n,m} e^{i(n\omega_{QP_2} + m\omega_{QP_3})t} \tag{3.1}$$

where $n, m \in \mathbb{N}$, ω_{QP_2} and ω_{QP_3} are the fundamental frequencies of QP. The blue dotted lines show the nonlinear frequency of LC_2 and the red dashed lines that of LC_3 at the corresponding values of Re.

We now interpret the spectra of figure 14 in the context of the bifurcation diagram of figure 4. Because $Re = 4420$ is close to Re_3', the quasiperiodic state at $Re = 4420$ is close to the limit cycle LC_3. In agreement with this, the peak at ω_{QP_3} matches almost exactly the nonlinear frequency $\omega_3 = 10.38$ of LC_3 indicated by the red dashed line in figure 14(a). In contrast QP is not close to LC_2 at this Reynolds number and so the peak at ω_{QP_2} is to the left of the the frequency $\omega_2 = 7.58$ of LC_2 (blue dotted line). At figure 14(c), corresponding to $Re = 4580$ near Re_2', the situation is naturally reversed. The peak at ω_{QP_2} matches almost exactly its analogue $\omega_2 = 7.634$ on LC_2 (blue dotted line) since it is close to LC_2, while ω_{QP_3} is slightly to the right of $\omega_3 = 10.445$ of LC_3. Away from LC_2 and LC_3 at $Re = 4500$, both frequencies $\omega_2 = 7.609$ and $\omega_3 = 10.412$ are slightly shifted from their analogues on the quasiperiodic state.

We have found from the nonlinear simulations that LC_2 loses stability towards LC_3 for $Re > Re_2' \approx 4600$ and LC_3 gains stability for $Re > Re_3' \approx 4420$. To shed light on the stability of these limit cycles, we carry out a Floquet analysis. In the Floquet framework, we decompose the velocity field as

$$\boldsymbol{U}(x,y,t) = \boldsymbol{U}_{\mathrm{LC}}(x,y,t) + \epsilon e^{(\sigma_F + i\omega_F)t} \boldsymbol{u}_F(x,y,t) + c.c. \tag{3.2}$$

with $\boldsymbol{U}_{\mathrm{LC}}$ the periodic solution corresponding to the limit cycle about which the Floquet analysis is performed, $\mathbf{u}_F$ the Floquet mode which is also periodic with period $T_b = 2\pi/\omega_b$ and $\sigma_F + i\omega_F$ the Floquet exponent. We rewrite (3.2) by expressing the Floquet mode as a Fourier series, leading to

$$\boldsymbol{U}(x,y,t) = \boldsymbol{U}_{\mathrm{LC}}(x,y,t) + \epsilon e^{(\sigma_F + i\omega_F)t} \sum_n \boldsymbol{u}_{F,n}(x,y) e^{in\omega_b t} + c.c. \tag{3.3}$$

For $t = T_b = \frac{2\pi}{\omega_b}$, $e^{in\omega_b T_b} = e^{in2\pi} = 1$ and so (3.3) becomes

$$\boldsymbol{U}(x,y,T_b) = \boldsymbol{U}_{\mathrm{LC}}(x,y,T_b) + \epsilon e^{\sigma_F 2\pi/\omega_b} e^{i2\pi\omega_F/\omega_b} \sum_n \boldsymbol{u}_{F,n}(x,y) + c.c. \tag{3.4}$$

with $\mu \equiv e^{\sigma_F 2\pi/\omega_b}$ the modulus and $\theta \equiv 2\pi\omega_F/\omega_b$ the argument of the Floquet multipliers.

Figure 15 shows the Floquet multipliers for both limit cycles in the complex plane. All Floquet multipliers (dots) are inside the unit circle, meaning that the corresponding limit cycles are stable at these Reynolds numbers. Figures 15(a,b) show the results for LC_2 at $Re = 4500$ and 4600 respectively. In figure 15a at $Re = 4500$, the dominant Floquet multiplier modulus is $|\mu| = 0.981$. On figure 15b, by $Re = 4600 \lesssim Re_2'$, this multiplier has moved closer to the unit circle, with $|\mu| = 0.999$. Figures 15(c,d) show that the moduli of the dominant Floquet multipliers for LC_3 at $Re = 4420 \gtrsim Re_3'$ and at $Re = 4500$ are $|\mu| = 0.967$ and $|\mu| = 0.995$. Thus the results shown by the Floquet analysis confirm the nonlinear observations.

We now turn to the argument of the Floquet multipliers. If the Floquet exponent is

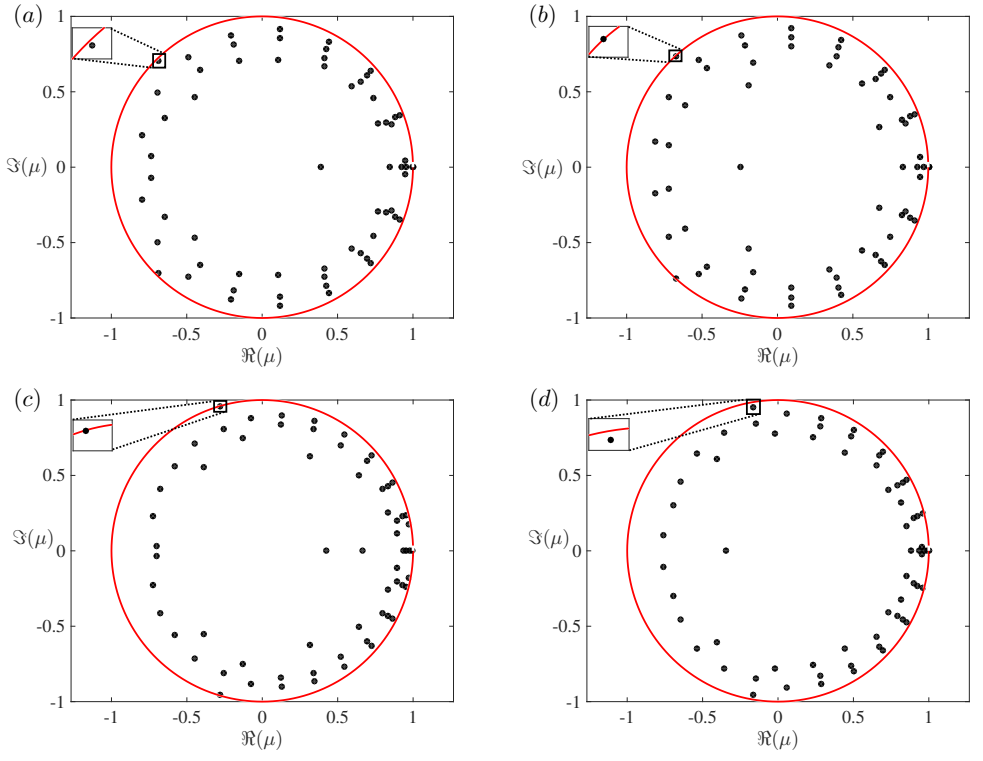

FIGURE 15. Floquet multipliers for LC_2 : (a) Re = 4500, (b) Re = 4600, and LC_3 : (c) Re = 4420, (d) Re = 4500. The small boxes are enlargements of the region surrounding the dominant Floquet multiplier.

real ($\omega_F = 0$) then the Floquet multiplier is one and the bifurcating state has the same frequency as the base limit cycle. If $\omega_F/\omega_b = 1/2$ then the Floquet multiplier is -1, which corresponds to a subharmonic mode. In our problem the dominant Floquet multiplier is complex, and so the bifurcation is a secondary Hopf bifurcation and the solution near the threshold of QP is described by equation (3.3). The spectrum of QP near the threshold contains ω_b and its multiples as well as the frequencies introduced by the secondary Hopf bifurcation, namely $\pm\omega_F \pm n\omega_b$, with a dominant contribution from $n = \pm 1$. Indeed, near Re'_2, the spectrum of QP contains frequencies ω_2 and $\omega_2 + \omega_F = \omega_2(1 + \frac{\theta}{2\pi}) = 10.45$ while near Re'_3, QP contains frequencies ω_3 and $\omega_3 - \omega_F = \omega_3(1 - \frac{\theta}{2\pi}) = 7.37$

These calculations are confirmed by figures 14(a,c) For (a) $Re = 4420 \gtrsim Re'_3$, the Floquet analysis about LC_3 yields a frequency $\omega_3 - \omega_F$ (solid vertical black line) comparable to the peak at ω_{QP_2} For (c) $Re = 4580 \lesssim Re'_2$, the Floquet analysis about LC_2 yields the frequency $\omega_2 + \omega_F$ (dashed vertical black line) which is very close to ω_{QP_3}.

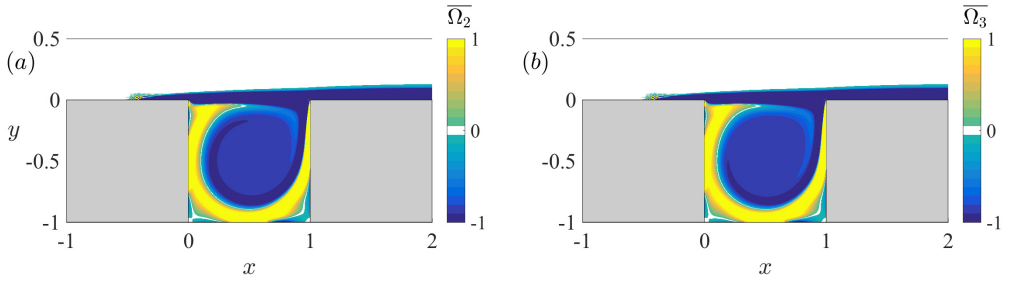

FIGURE 16. Mean flows ($\overline{\Omega_2}$, $\overline{\Omega_3}$) at $Re = 4500$ for (a) LC_2 and (b) LC_3 . The difference between the mean flow of LC_2 and LC_3 is not visible. Nor is there any visible change between the mean and base flows shown in figure 5.

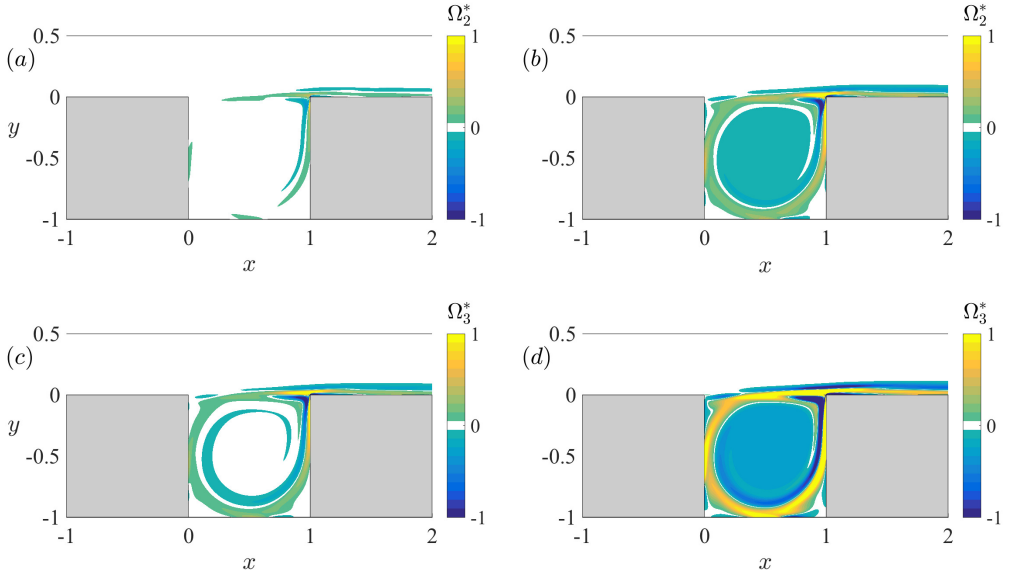

FIGURE 17. Distortion of the mean flow ($\Omega^* = \overline{\Omega} - \Omega_b$). For LC_2 at (a) $Re = 4200$ and (b) $Re = 4500$. For LC_3 at (c) $Re = 4500$ and (d) $Re = 5000$. Figures 17b,c corresoond to 16a,b. The distortion measures the deviation of the mean flow from the base flow due to nonlinear interaction and increases with Reynolds number.

4. Frequency prediction

4.1. *Linearization about the mean flow*

Linear stability analysis – i.e. linearizing about the base flow and solving the resulting eigenproblem – is a classic tool in hydrodynamics. Bifurcations which create new branches are determined unambiguously by linear stability analysis and, if the bifurcation is supercritical, the spatial and temporal behaviors of the new states near threshold are similar to those of the eigenvector and eigenvalue responsible for the instability. Further from the threshold, these properties evolve and may well differ substantially from those of the bifurcating eigenvector and eigenvalue. In some such cases, it has been shown that linearization about the mean flow of a limit cycle can yield more accurate approximations of the nonlinear states. We have carried out a linear analysis about the temporal mean for both limit cycles LC_2 and LC_3 and compared the resulting frequencies with those obtained from linearization about the base flow and with the nonlinear frequencies of

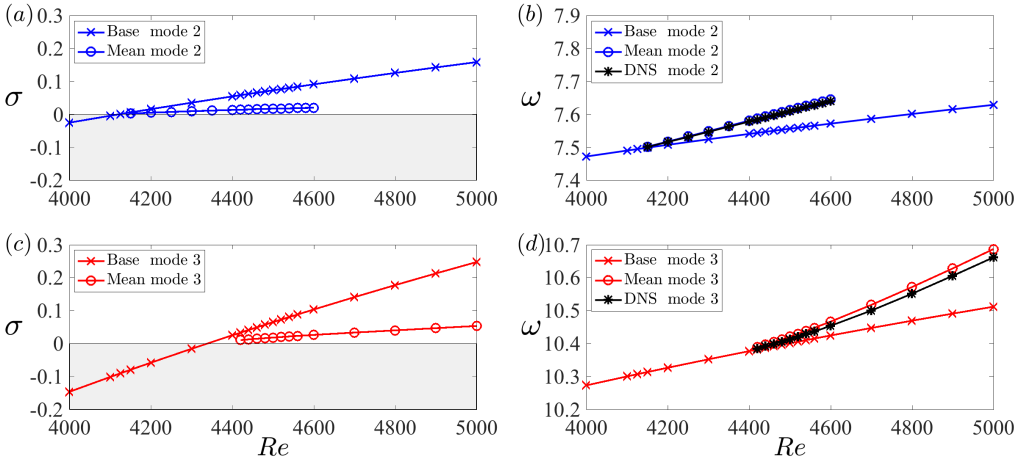

FIGURE 18. Eigenvalues $\sigma + i\omega$ from linear stability analysis about the base and mean flows of LC_2 and LC_3. The eigenvalues about the base flow are plotted with crosses. Linear stability about the mean flow is shown with circles. The nonlinear frequency from DNS is plotted with black stars. (a,c): The growth rate σ for LC_2 for the mean flow is nearly zero but that of LC_3 is smaller than that about the base flow, but not enough to be considered to be neutrally stable. (b,d): The imaginary parts of the eigenvalues are almost exactly equal to the nonlinear frequencies, especially for LC_2. For LC_3, although the imaginary part of the eigenvalue and the nonlinear frequency are necessarily equal at onset, the two diverge slightly as Re increases.

these cycles. This procedure has been carried out for LC_3 by Meliga (2017); here we carry out the same procedure for LC_2 and compare the two regimes.

In figure 16 we show the vorticity of the mean flow for LC_2 and LC_3 at $Re = 4500$, which is in the overlap region where both limit cycles exist and are stable. The base flow dominates the mean flow and therefore the difference is made visible by plotting the distortion $\overline{\Omega}^* = \overline{\Omega} - \Omega_b$, which is shown for LC_2 at $Re = 4200$ and 4500 in figure 17(a,b) and for LC_3 at $Re = 4500$ and 5000 in figure 17(c,d).

Figure 18 and Tables 1 and 2 compare the results of linearization about the base flow and the mean flow and those of the nonlinear simulation. Figure 18 plots the frequencies and growth rates over the Reynolds number range $[4000, 5000]$ that we have studied, while Tables 1 and 2 shows numerical data extracted from these figures for three representative Reynolds numbers, 4200, 4500 and 5000. We note that unlike for the cylinder wake Barkley (2006), the frequencies obtained from the usual linear stability analysis are already not very far from those of the nonlinear limit cycles. Table 1 shows a deviation of less than 0.6% for the frequencies in LC_2 and of less than 1.4% for LC_3 over this Reynolds number range. In contrast, for the cylinder wake (Barkley 2006), the difference between the nonlinear frequencies and those obtained by linear stability analysis reaches 15% by $Re = 60$, a Reynolds number comparable to the distance above criticality studied here and reaches 100% by $Re = 180$, a frequent upper limit of such studies.

Figure 18(b) for LC_2 (circles) shows that the frequency obtained by linearization about the mean flow is nonetheless much closer to the nonlinear temporal frequency (stars) than that given by linear stability about the base flow (crosses). Quantitatively, table 1 shows the relative difference at $Re = 4500$ between the nonlinear frequency and the frequency obtained from the base flow to be 0.7%; this difference is reduced to 0.04% when the linearization is performed about the mean flow. Moreover, the growth rate obtained

	linearize about base			linearize about mean			nonlinear			$\Delta\omega$	Δf
Re	4200	4500	5000	4200	4500	5000	4200	4500	5000		
ω_2	7.502	7.556	7.629	7.517	7.612		7.516	7.609		2.8	0.45
	0.014	0.053		0.001	0.003						
ω_3	10.327	10.401	10.512		10.421	10.686		10.412	10.661	2.8	0.45
		0.011	0.149		0.009	0.025					
ω_4	13.099	13.188	13.321							2.8	0.45
ω_5	15.931	16.029	16.183								

TABLE 1. Linear and nonlinear frequencies for cavity modes. Frequencies from linearization about the base and from linearization about the mean and nonlinear simulations, where available. Second row for ω_2 and ω_3 shows deviation from frequencies from nonlinear simulations. When the RZIF property is satisfied, linearization about the nonlinear mean yields frequencies close to nonlinear frequencies. Last columns show the frequency increment from one row to the next row, which is constant to two digits, regardless of the Reynolds number or which type of frequency is used.

	linearize about base			linearize about mean		
Re	4200	4500	5000	4200	4500	5000
σ_2	0.016	0.073	0.158	0.005	0.017	
σ_3	−0.058	0.065	0.247		0.018	0.053

TABLE 2. Linear growth rates for cavity modes. Linearization about base yields growth rates which cross zero transversely as the bifurcation threshold is crossed. When the RZIF property is satisfied, linearization about the nonlinear mean yields growth rates near zero, i.e. the mean flow is nearly marginally stable.

about the mean flow (circles) in figure 18(a) is nearly zero, as found by Barkley (2006) for the cylinder wake. Table 2 shows a growth rate at $Re = 4500$ of 0.073 for linearization about the base flow; this is reduced by a factor of 5 to 0.017 for the linearization about the mean.

For LC_3, the frequency obtained by linearizing about the mean presented in figure 18(d) (circles) agrees well with the nonlinear frequency (stars). The curves begin to diverge slightly for $Re \geqslant 4600$, and although the agreement is not as good as it is for LC_2, the frequencies are still very close. Quantitatively, table 1 shows the relative difference at $Re = 5000$ between the nonlinear frequency and the frequency obtained from the base flow to be 1.4%; this difference is reduced to 0.02% when the linearization is performed about the mean flow. Table 2 shows a growth rate at $Re = 5000$ of 0.247 for linearization about the base flow; this is reduced by a factor of 5 to 0.053 for the linearization about the mean.

Figure 19 shows the vertical velocity of the real and imaginary parts of the leading

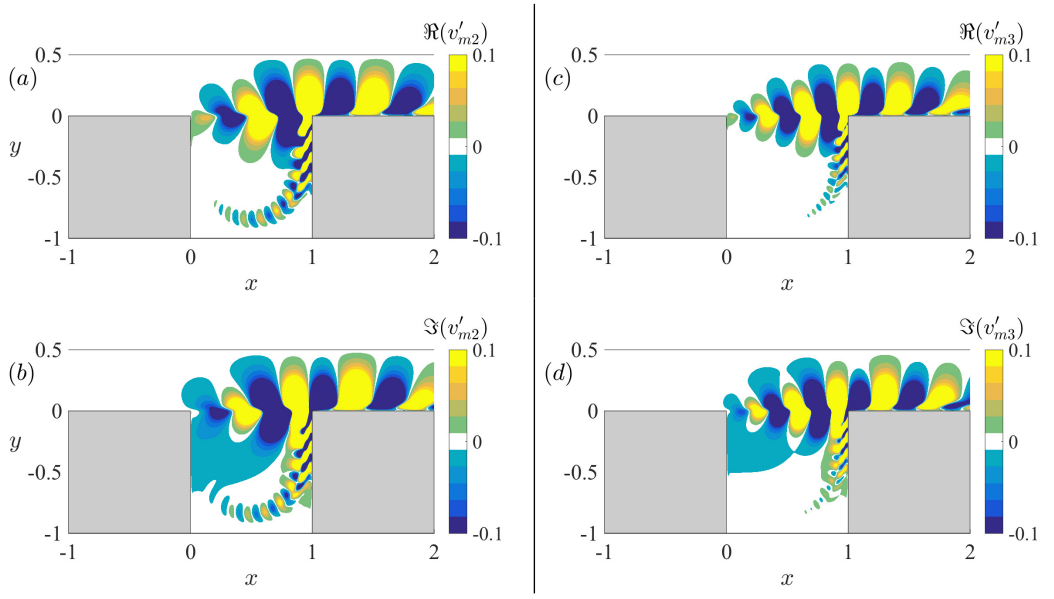

FIGURE 19. Real and imaginary parts of the leading unstable eigenmodes about the mean flow for the vertical velocity at $Re = 4500$. (a,b) LC_2 and (c,d) LC_3.

eigenmode at $Re = 4500$ for LC_2 (a,c) and LC_3 (b,d). These modes, with two and three vortex pairs, respectively, resemble those about the base flow (figure 11) and also resemble the nonlinear vertical velocity fluctuations figures 7 and 8.

Like the base flow, a mean flow has a full spectrum of eigenvalues and eigenvectors. Thus, the mean flow of LC_2 has not only the eigenvectors with two vortex pairs shown in 19(a,b) with corresponding eigenvalues shown in figures 18(a,b), resembling those which lead to LC_2, but it also has also eigenvectors with three pairs of vortices resembling those which lead to LC_3 and their corresponding eigenvalues. Similarly, the mean flow of LC_3 has eigenvectors containing two vortex pairs. We refer to these as cross-eigenvalues. Referring back to figure 4(b), these eigenvalues correspond to the horizonal arrows emanating to or from LC_2, located on the vertical axis, and the vertical arrows emanating to or from LC_3, located on the horizontal axis.

Figure 20 shows the cross-eigenvalues corresponding to mode two, obtained by linearization about the mean flow of LC_3 (circles, figure 20(a,b) and those of mode three about the mean flow of LC_2 (circles, figure 20(c,d). The eigenvalues obtained from the base and from the mean necessarily agree at Re_2 for LC_2 and at Re_3 for LC_3, since when the limit cycles are created, the base and mean flows are equal.

Focusing on figure 20(a), we recall that LC_3 is created at $Re_3 \approx 4348$ and is unstable to eigenmodes of type 2 until $Re'_3 \approx 4410$, i.e. this cross-eigenvalue is positive for $Re \in [4348, 4410]$. This is qualitatively the behavior that is seen in figure 20(a), although here σ is positive over a higher range, for $Re \in [4410, 4681]$. Focusing now on figure 20(c), we recall that LC_2 is created at $Re_2 \approx 4126$ and becomes unstable to eigenmodes of type 3 at $Re'_2 \approx 4600$. This is again qualitatively close to the behavior is seen in figure 20(c), except that here σ becomes positive at the lower value of $Re \approx 4418$.

These results indicate that for a limit cycle, linearization about its mean flow may be able to convey information about the growth rate, frequency, and spatial characteristics of its stability to secondary bifurcations. Although this is certainly a plausible idea, to our knowledge it has not previously been reported.

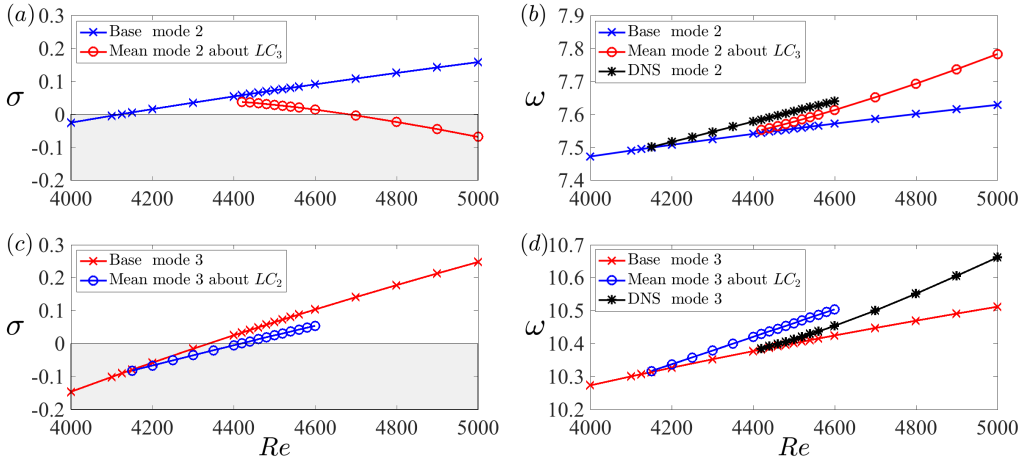

FIGURE 20. Eigenvalues $\sigma + i\omega$ from linearization about the base and mean flows. Here the spatial form of the eigenvector does not correspond to that of the mean flow. The eigenvalues about the base flow are plotted with crosses, blue for LC_2 and red for LC_3. The eigenvalues of mode two about the mean flow of LC_3 are shown with red circles and that of mode three about the mean flow of LC_2 with blue circles. The nonlinear frequencies from DNS are plotted with black stars for LC_2 and LC_3. *(a)* The growth rate of mode two about the mean of LC_3 (red circles) decreases from the threshold $Re_3 \approx 4348$ of LC_3 and becomes negative at $Re \approx 4681$. This may correspond qualitatively to the fact that LC_3 is unstable to mode 2 perturbations when it is created at Re_3 and becomes stable at $Re_3' \approx 4410$. *(c)* The growth rate of mode three about the mean of LC_2 (blue circles) increases from the threshold Re_2 of LC_2 and becomes positive at $Re \approx 4418$. This may correspond qualitatively to the fact that LC_2 is stable when created at $Re_2 \approx 4126$ and becomes unstable at $Re_2' \approx 4600$.

4.2. *RZIF and SCM*

We now present an argument for the validity of linearization about the mean flow. Turton *et al.* (2015) argued that the RZIF property holds exactly if the time dependence is monochromatic, meaning that higher harmonics are negligible compared to the fundamental frequency. Consider the evolution equation

$$\partial_t \boldsymbol{U} = \mathcal{L}\boldsymbol{U} + \mathcal{N}(\boldsymbol{U}, \boldsymbol{U}) \tag{4.1}$$

where $\mathcal{L}$ is linear and $\mathcal{N}(\cdot,\cdot)$ is a quadratic nonlinearity. Let

$$\boldsymbol{U} = \overline{\boldsymbol{U}} + \sum_{n\neq 0} \boldsymbol{u}_n e^{in\omega t} \tag{4.2}$$

(with $\boldsymbol{u}_{-n} = \boldsymbol{u}_n^*$) be the temporal Fourier decomposition of a periodic solution to (4.1) with mean $\overline{\boldsymbol{U}}$ and frequency ω. The $n = 0$ (mean) component of (4.1) is

$$0 = \mathcal{L}\overline{\boldsymbol{U}} + \mathcal{N}(\boldsymbol{u}_1, \boldsymbol{u}_{-1}) + \mathcal{N}(\boldsymbol{u}_{-1}, \boldsymbol{u}_1) + \mathcal{N}(\boldsymbol{u}_2, \boldsymbol{u}_{-2}) + \mathcal{N}(\boldsymbol{u}_{-2}, \boldsymbol{u}_2) + \dots \tag{4.3}$$

while the $n = 1$ component is

$$\begin{aligned} i\omega \boldsymbol{u}_1 = &\underbrace{\mathcal{L}\boldsymbol{u}_1 + \mathcal{N}(\overline{\boldsymbol{U}}, \boldsymbol{u}_1) + \mathcal{N}(\boldsymbol{u}_1, \overline{\boldsymbol{U}})}_{\mathcal{L}_{\overline{U}}\boldsymbol{u}_1} \\ &+ \underbrace{\mathcal{N}(\boldsymbol{u}_2, \boldsymbol{u}_{-1}) + \mathcal{N}(\boldsymbol{u}_{-1}, \boldsymbol{u}_2) + \mathcal{N}(\boldsymbol{u}_3, \boldsymbol{u}_{-2}) + \mathcal{N}(\boldsymbol{u}_{-2}, \boldsymbol{u}_3) + \dots}_{\mathcal{N}_1} \end{aligned} \tag{4.4}$$

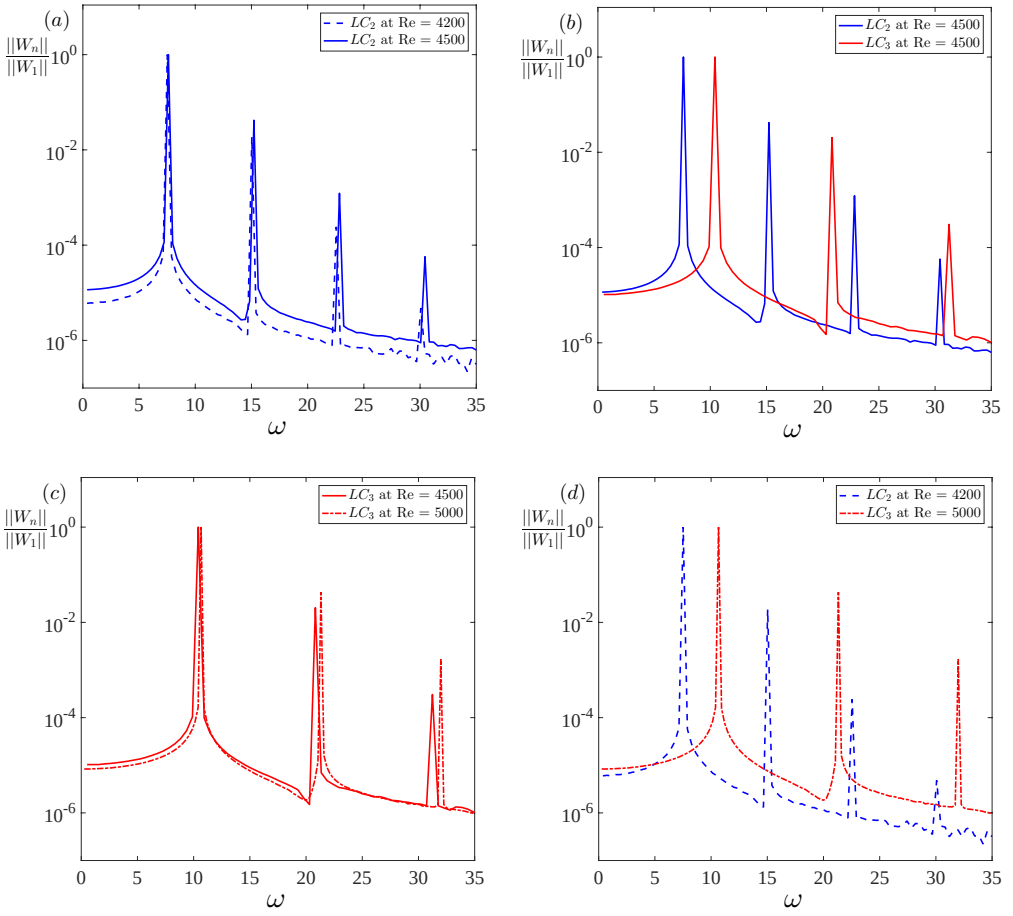

FIGURE 21. Temporal spectra of streamwise velocity normalized by the fundamental frequency for LC_2 and LC_3. (a) Spectra of LC_2 at $Re = 4200$ and $Re = 4500$. (b) At $Re = 4500$ for LC_2 and LC_3. (c) At $Re = 4500$ and $Re = 5000$ for LC_3. (d) Spectra of LC_2 and LC_3 at $Re = 4200$ and $Re = 5000$ respectively.

If, as is often the case, $||u_n|| \sim \epsilon^{|n|}$, then $\mathcal{N}_1 = O(\epsilon^3)$ may be neglected and RZIF is satisfied: the linear operator $\mathcal{L}_{\overline{U}}$ in (4.4) has the pure imaginary eigenvalue $i\omega$, corresponding to the frequency of the periodic solution. Hence the RZIF property is satisfied for near-monochromatic oscillations in a system with quadratic nonlinearity.

We mention here that RZIF is not predictive, since it requires a full nonlinear direct numerical simulation to be carried out in order to compute the temporal mean $\overline{U}$. An approach which is actually predictive, i.e. which does not require a DNS, called the Self-Consistent Model (SCM) has been proposed by Mantič-Lugo *et al.* (2014, 2015). The SCM truncates the mean flow equation (4.3) as well as the $n = 1$ equation (4.4), leading to the closed system

$$\begin{aligned} 0 &= \mathcal{L}\overline{\boldsymbol{U}} + \mathcal{N}(\boldsymbol{u}_1, \boldsymbol{u}_{-1}) + \mathcal{N}(\boldsymbol{u}_{-1}, \boldsymbol{u}_1) \\ i\omega\boldsymbol{u}_1 &= \mathcal{L}\boldsymbol{u}_1 + \mathcal{N}(\overline{\boldsymbol{U}}, \boldsymbol{u}_1) + \mathcal{N}(\boldsymbol{u}_1, \overline{\boldsymbol{U}}) \end{aligned} \tag{4.5}$$

This system is then solved for $\overline{\boldsymbol{U}}$ and $\boldsymbol{u}_1$ by various iterative methods; see Mantič-Lugo *et al.* (2014, 2015). The next higher truncation, i.e. retaining $\overline{\boldsymbol{U}}$, $\boldsymbol{u}_1$, and $\boldsymbol{u}_2$, has

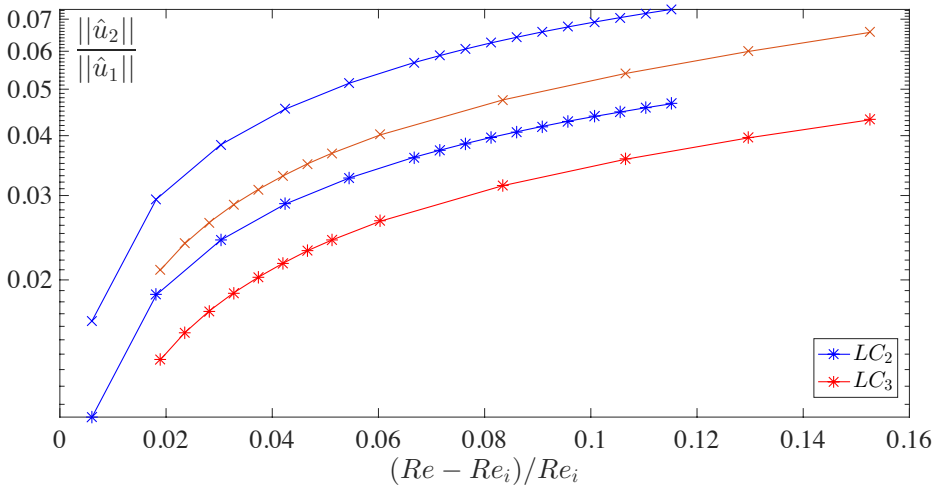

FIGURE 22. Amplitude of second harmonic (stars) and the sum of the amplitudes of the three lowest harmonics (crosses) normalized by the amplitude of the fundamental frequency as a function of relative Reynolds number for LC_2 and LC_3. As in figure 21, the fundamental frequency dominates the second harmonic. These ratios are always below 10^{-1} and are slightly higher for LC_2 than that for LC_3.

been studied by Meliga (2017). It may happen, however, that RZIF is satisfied, while SCM is not, i.e. that while higher-order modes may be neglected in (4.4), they are essential to forming the correct mean flow and cannot be neglected in (4.3); see Bengana & Tuckerman (2018*a*).

For thermosolutal convection, Turton *et al.* (2015) showed that for traveling waves, the RZIF property is satisfied and the spectrum is highly peaked, while for standing waves the spectrum is broad and the RZIF property is not satisfied. We now wish to see if the temporal spectra of LC_2 and LC_3 also explain the fact that the RZIF property is better satisfied for LC_2 than for LC_3. We show in figure 21 the temporal spectra of streamwise velocity normalized by the fundamental frequency for LC_2 and LC_3, for various values of Reynolds number. In figure 22 we plot the ratio of the second harmonic to the fundamental frequency. The ratio $||\hat{u}_2||/||\hat{u}_1||$ is consistently less than 0.05 for both flows over the range of our investigation, while $(||\hat{u}_2|| + ||\hat{u}_3|| + ||\hat{u}_4||/||\hat{u}_1||$ remains below 0.07, consistent with the fact that RZIF is satisfied. We observed that RZIF is closer to being valid for LC_2 than for LC_3, but the ratios in figure 22 follow the opposite tendency. Thus, the explanation proposed by Turton *et al.* (2015) in terms of the temporal Fourier amplitudes does not explain this difference.

4.3. *Rossiter formula*

We return to Table 1, the last column of which shows that the frequencies of successive modes by a constant interval. (For a given frequency, the various versions of its value differ by at most 1%-2%.) We emphasize this again by reproducing the eigenspectra in figure 23, adding horizontal lines which emphasize visually the constant difference between the frequencies. In flows over shear-driven cavities, Rossiter (1964) observed that the temporal frequencies for self-sustained oscillations were quantized and proposed the following empirical formula:

$$f_n = \frac{U_\infty}{L}\frac{n-\gamma}{M+1/\kappa} \quad \Longrightarrow \quad \frac{U_\infty}{L}\kappa\,(n-\gamma) \text{ for } M=0 \tag{4.6}$$

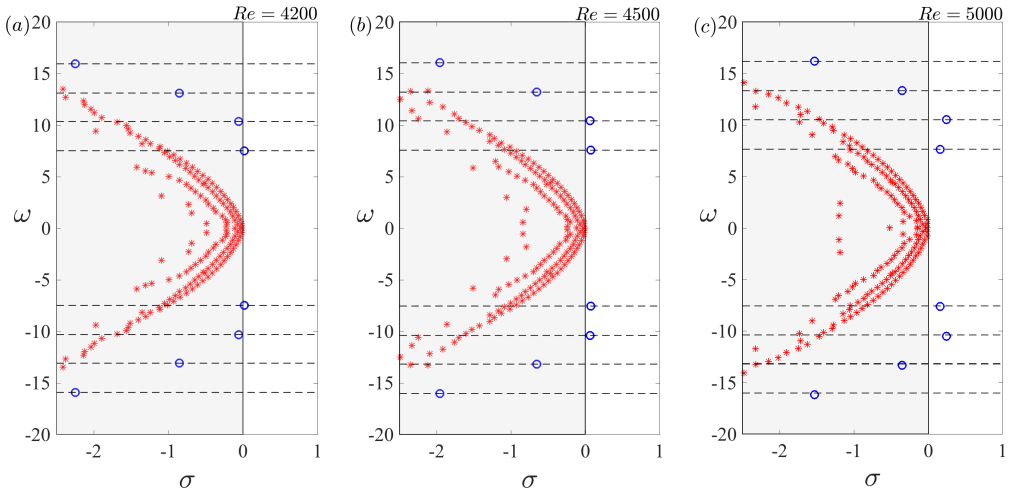

FIGURE 23. Spectra of the base flow for (*a*) $Re = 4200$, (*b*) $Re = 4500$, (*c*) $Re = 5000$. Blue circles designate the converged eigenvalues and red stars the eigenvalues that did not converge. Horizontal lines emphasize the fact that the frequencies are equally spaced.

where U_∞ and L are the free-stream speed away from the cavity and the length of the cavity, and M is the Mach number, here set to zero. The phenomenological constant γ is a phase lag, while the increment κ will be discussed below. The essence of (4.6) is not only that the temporal frequencies f_n observed are quantized (which is to be expected in a finite cavity) but that they are separated by a fixed increment Δf. Heuristically, if the limit cycle consists of n vortex pairs advected horizontally at velocity U_{adv}, then the average vortex pair occupies a length L/n and strikes the cavity corner with frequency $U_{\mathrm{adv}}/(L/n)$. Since the frequencies in table 1 are nondimensionalized by U_∞/L, we have

$$\Delta f = \frac{U_\infty}{L}\kappa = \frac{U_{\mathrm{adv}}}{L} = 0.45 \quad \Longrightarrow \quad \kappa = \frac{U_{\mathrm{adv}}}{U_\infty} = 0.45 \tag{4.7}$$

5. Conclusion

We have carried out a detailed study of the dynamics of shear-driven square cavity flow over the Reynolds number range 4000 to 5000. An original result of the study is the detailed description of two solution branches, which are limit cycles with different numbers of vortices and which appear by successive primary supercritical Hopf bifurcations. Stability is transferred from the first to the second limit cycle via an unstable quasiperiodic state which is created and destroyed via subcritical secondary Hopf bifurcations from the limit cycles. The primary and secondary Reynolds numbers are such that there exists a region of bistability. Transition from one limit cycle to the other is hysteretic and is characterized by a sudden change in frequency from $\omega \sim 7$ to $\omega \sim 10$ and a change in the number of vortex pairs along the shear layer of the cavity. By using edge state tracking, we have been able to produce an approximation to the quasiperiodic state and to measure its temporal Fourier spectrum, which corresponds well to the frequencies computed via a Floquet analysis of the two limit cycles.

Our second focus has been to apply the technique of linearization about the temporal mean of the limit cycles, an approach which has been shown to describe nonlinear

properties in many cases. More specifically, in many cases the real part of the leading eigenvalue is near zero (a property which would be described as marginal stability in the context of linearization about the base) and the imaginary part is near the nonlinear frequency of the limit cycles. The combination of these properties is called RZIF. This technique has been studied most extensively for the wake of a circular cylinder, for which the nonlinear frequencies deviate substantially from those obtained by linearization about the base flow. For shear-driven cavity flow, the frequencies of the nonlinear limit cycles are not very far from those derived by linearization about the base flow, but linearization about the mean flow substantially reduces this already small difference. However, RZIF is not verified as spectacularly as it is for the cylinder wake, as has already been documented by Sipp & Lebedev (2007) and Meliga (2017). Because the shear-driven cavity flow in our Reynolds number range has two limit cycles, we can take the further step of computing other eigenmodes of the mean, which do not correspond to the limit cycle. We find that these eigenmodes mimic qualitatively the behavior of the limit cycles with respect to one other: as the Reynolds number is increased, the real part of one eigenvalue decreases from positive to negative for a limit cycle which undergoes stablization via a secondary bifurcation, and increases from negative to positive for a cycle which undergoes destabilization.

In summary, the existence of two competiting limit cycles for shear-driven cavity flow has yielded both an interesting bifurcation diagram, containing features such as subcritical bifurcations, hysteresis and a quasiperiodic state. At the same time, the existence of two cycles has also extended the application and interpretation of linearization about the mean flow.

Acknowledgments

This work was performed using high performance computing resources provided by the Institut du Developpement et des Ressources en Informatique Scientifique (IDRIS) of the Centre National de la Recherche Scientifique (CNRS), coordinated by GENCI (Grand Équipement National de Calcul Intensif), grants A0032A06362 and A0042A01119.

REFERENCES

Åkervik, E., Brandt, L., Henningson, D. S., Hœpffner, J., Marxen, O. & Schlatter, P. 2006 Steady solutions of the Navier-Stokes equations by selective frequency damping. *Phys. Fluids* **18** (6), 068102.

Barbagallo, Alexandre, Sipp, Denis & Schmid, Peter J 2009 Closed-loop control of an open cavity flow using reduced-order models. *J. Fluid Mech.* **641**, 1–50.

Barkley, D 2006 Linear analysis of the cylinder wake mean flow. *EPL (Europhysics Letters)* **75** (5), 750.

Barkley, Dwight & Henderson, Ronald D 1996 Three-dimensional Floquet stability analysis of the wake of a circular cylinder. *J. Fluid Mech.* **322**, 215–241.

Basley, J., Pastur, L. R., Delprat, N. & Lusseyran, F. 2013 Space-time aspects of a three-dimensional multi-modulated open cavity flow. *Phys. Fluids* **25**, 064105.

Beneddine, Samir, Sipp, Denis, Arnault, Anthony, Dandois, Julien & Lesshafft, Lutz 2016 Conditions for validity of mean flow stability analysis. *J. Fluid Mech.* **798**, 485–504.

Bengana, Y. & Tuckerman, L.S. 2018*a* The self-consistent model and thermosolutal convection. *in preparation* .

Bengana, Y. & Tuckerman, L.S. 2018*b* Spirals and ribbons: frequencies from mean flows and heteroclinic orbits. *submitted* .

Chien, W-L, Rising, H & Ottino, JM 1986 Laminar mixing and chaotic mixing in several cavity flows. *J. Fluid Mech.* **170**, 355–377.

Cunha, G, Passaggia, P-Y & Lazareff, M 2015 Optimization of the selective frequency damping parameters using model reduction. *Phys. Fluids* **27** (9), 094103.

Duguet, Yohann, Willis, Ashley P & Kerswell, Rich R 2008 Transition in pipe flow: the saddle structure on the boundary of turbulence. *J. Fluid Mech.* **613**, 255–274.

Edwards, WS, Tuckerman, Laurette S, Friesner, Richard A & Sorensen, DC 1994 Krylov methods for the incompressible Navier-Stokes equations. *J. Comput. Phys.* **110** (1), 82–102.

Fani, A, Citro, V, Giannetti, F & Auteri, F 2018 Computation of the bluff-body sound generation by a self-consistent mean flow formulation. *Phys. Fluids* **30** (3), 036102.

Fischer, P.F., Lottes, J.W. & Kerkemeir, S.G. 2008 Nek5000 Web pages. Http://nek5000.mcs.anl.gov.

Gioria, Rafael dos Santos, Jabardo, Paulo José Saiz, Carmo, Bruno Souza & Meneghini, Julio Romano 2009 Floquet stability analysis of the flow around an oscillating cylinder. *J. Fluids Struct.* **25** (4), 676–686.

Gloerfelt, Xavier 2009 Cavity noise. *VKI lecture series* **3**.

Hammond, DA & Redekopp, LG 1997 Global dynamics of symmetric and asymmetric wakes. *J. Fluid Mech.* **331**, 231–260.

Itano, Tomoaki & Toh, Sadayoshi 2001 The dynamics of bursting process in wall turbulence. *JPSJ* **70** (3), 703–716.

Jordi, B E, Cotter, C J & Sherwin, S J 2014 Encapsulated formulation of the selective frequency damping method. *Phys. Fluids* **26** (3), 034101.

Jordi, B E, Cotter, C J & Sherwin, S J 2015 An adaptive selective frequency damping method. *Phys. Fluids* **27** (9), 094104.

Liu, Q., Gmez, F. & Theofilis, V. 2016 Linear instability analysis of low-Re incompressible flow over a long rectangular finite-span open cavity. *J. Fluid Mech.* **799**, R2.

Loiseau, J-Ch & Brunton, S L 2018 Constrained sparse Galerkin regression. *J. Fluid Mech.* **838**, 42–67.

Lopez, Juan M, Welfert, Bruno D, Wu, Ke & Yalim, Jason 2017 Transition to complex dynamics in the cubic lid-driven cavity. *Phys. Rev. Fluids* **2** (7), 074401.

Malkus, W. V. R. 1956 Outline of a theory of turbulent shear flow. *J. Fluid Mech.* **1** (5), 521–539.

Mantič-Lugo, Vladislav, Arratia, Cristóbal & Gallaire, François 2014 Self-consistent mean flow description of the nonlinear saturation of the vortex shedding in the cylinder wake. *Phys. Rev. Lett.* **113** (8), 084501.

Mantič-Lugo, Vladislav, Arratia, Cristóbal & Gallaire, François 2015 A self-consistent model for the saturation dynamics of the vortex shedding around the mean flow in the unstable cylinder wake. *Phys. Fluids* **27** (7), 074103.

Maurel, A, Pagneux, V & Wesfreid, JE 1995 Mean-flow correction as non-linear saturation mechanism. *Europhys. Lett.* **32** (3), 217.

McKeon, BJ & Sharma, AS 2010 A critical-layer framework for turbulent pipe flow. *J. Fluid Mech.* **658**, 336–382.

Meliga, Philippe 2017 Harmonics generation and the mechanics of saturation in flow over an open cavity: a second-order self-consistent description. *J. Fluid Mech.* **826**, 503–521.

Meliga, Philippe, Boujo, Edouard & Gallaire, François 2016 A self-consistent formulation for the sensitivity analysis of finite-amplitude vortex shedding in the cylinder wake. *J. Fluid Mech.* **800**, 327–357.

Mittal, Sanjay 2008 Global linear stability analysis of time-averaged flows. *Int. J. Numer. Meth. Fluids* **58** (1), 111–118.

Morris, P. J. 1976 The spatial viscous instability of axisymmetric jets. *J. Fluid Mech.* **77** (3), 511–529.

Picella, F., Loiseau, J.-Ch., Lusseyran, F, Robinet, J.-Ch., Cherubini, S. & Pastur, L. 2018 Successive bifurcations in a fully three-dimensional open cavity flow. *J. Fluid Mech.* **844**, 855–877.

Pier, Benoît 2002 On the frequency selection of finite-amplitude vortex shedding in the cylinder wake. *J. Fluid Mech.* **458**, 407–417.

Rockwell, D & Knisely, C 1980 Vortex-edge interaction: Mechanisms for generating low frequency components. *Phys. Fluids* **23** (2), 239–240.

Rockwell, D & Naudascher, Et 1978 Self-sustaining oscillations of flow past cavities. *Journal of Fluids Engineering* **100** (2), 152–165.

Rossiter, JE 1964 Wind tunnel experiments on the flow over rectangular cavities at subsonic and transonic speeds. *Tech. Rep.*. Ministry of Aviation; Royal Aircraft Establishment; RAE Farnborough.

Rowley, Clarence W, Colonius, Tim & Basu, Amit J 2002 On self-sustained oscillations in two-dimensional compressible flow over rectangular cavities. *J. Fluid Mech.* **455**, 315–346.

Schmid, P. J. 2010 Dynamic mode decomposition of numerical and experimental data. *J. Fluid Mech.* **656**, 5–28.

Sipp, Denis & Lebedev, Anton 2007 Global stability of base and mean flows: a general approach and its applications to cylinder and open cavity flows. *J. Fluid Mech.* **593**, 333–358.

Sipp, Denis, Marquet, Olivier, Meliga, Philippe & Barbagallo, Alexandre 2010 Dynamics and control of global instabilities in open-flows: a linearized approach. *Appl. Mech. Rev.* **63** (3), 030801.

Smith, Julius O. 2007 *Mathematics of the Discrete Fourier Transform (DFT)*. W3K Publishing.

Stuart, J. T. 1958 On the non-linear mechanics of hydrodynamic stability. *J. Fluid Mech.* **4** (1), 1–21.

Symon, Sean, Rosenberg, Kevin, Dawson, Scott TM & McKeon, Beverley J 2018 Non-normality and classification of amplification mechanisms in stability and resolvent analysis. *Phys. Rev. Fluids* **3** (5), 053902.

Turton, Sam E, Tuckerman, Laurette S & Barkley, Dwight 2015 Prediction of frequencies in thermosolutal convection from mean flows. *Phys. Rev. E* **91** (4), 043009.

Yamouni, S., Sipp, D. & Jacquin, L. 2013 Interaction between feedback aeroacoustic and acoustic resonance mechanisms in a cavity flow: a global stability analysis. *J. Fluid Mech.* **717**, 134–165.

Yu, Yung H 1977 Measurements of sound radiation from cavities at subsonic speeds. *J. Aircr* **14** (9), 838–843.

Zielinska, BJA, Goujon-Durand, S, Dusek, J & Wesfreid, JE 1997 Strongly nonlinear effect in unstable wakes. *Phys. Rev. Lett.* **79** (20), 3893.